The Astrophysical Journal, 848:132 (22pp), 2017 October 20 https://doi.org/10.3847/1538-4357/aa8f51

GASP. III. JO36: A Case of Multiple Environmental Effects at Play?

Jacopo Fritz[1], Alessia Moretti[2], Marco Gullieuszik[2], Bianca Poggianti[2], Gustavo Bruzual[1], Benedetta Vulcani[2,3], Fabrizio Nicastro[4], Yara Jaffé[5], Bernardo Cervantes Sodi[1], Daniela Bettoni[2], Andrea Biviano[5], Giovanni Fasano[2], Stéphane Charlot[6], Callum Bellhouse[7,8], and George Hau[8]

[1] Instituto de Radioastronomía y Astrofísica, UNAM, Campus Morelia, A.P. 3-72, C.P. 58089, Mexico; j.fritz@irya.unam.mx
[2] INAF-Osservatorio Astronomico di Padova, Vicolo dell'Osservatorio 5, Padova, Italy
[3] School of Physics, The University of Melbourne, Swanston St. & Tin Alley Parkville, VIC 3010, Australia
[4] INAF-Osservatorio Astronomico di Roma, Via di Frascati 33, I-00040 Monte Porzio Catone, RM, Italy
[5] INAF-Osservatorio Astronomico di Trieste, via G. B. Tiepolo 11, I-34131, Trieste, Italy
[6] Sorbonne Universités, UPMC-CNRS, UMR7095, Institut d'Astrophysique de Paris, F-75014 Paris, France
[7] University of Birmingham, School of Physics and Astronomy, Edgbaston, Birmingham, UK
[8] European Southern Observatory, Alonso de Cordova 3107, Vitacura, Casilla 19001, Santiago de Chile, Chile
Received 2017 April 13; revised 2017 September 15; accepted 2017 September 21; published 2017 October 24

Abstract

The so-called jellyfish galaxies are objects exhibiting disturbed morphology, mostly in the form of tails of gas stripped from the main body of the galaxy. Several works have strongly suggested ram pressure stripping to be the mechanism driving this phenomenon. Here, we focus on one of these objects, drawn from a sample of optically selected jellyfish galaxies, and use it to validate SINOPSIS, the spectral fitting code that will be used for the analysis of the GASP (GAs Stripping Phenomena in galaxies with MUSE) survey, and study the spatial distribution and physical properties of the gas and stellar populations in this galaxy. We compare the model spectra to those obtained with GANDALF, a code with similar features widely used to interpret the kinematics of stars and gas in galaxies from IFU data. We find that SINOPSIS can reproduce the pixel-by-pixel spectra of this galaxy at least as well as GANDALF does, providing reliable estimates of the underlying stellar absorption to properly correct the nebular gas emission. Using these results, we find strong evidences of a double effect of ram pressure exerted by the intracluster medium onto the gas of the galaxy. A moderate burst of star formation, dating between 20 and 500 Myr ago and involving the outer parts of the galaxy more strongly than the inner regions, was likely induced by a first interaction of the galaxy with the intracluster medium. Stripping by ram pressure, plus probable gas depletion due to star formation, contributed to create a truncated ionized gas disk. The presence of an extended stellar tail on only one side of the disk points instead to another kind of process, likely gravitational interaction by a fly-by or a close encounter with another galaxy in the cluster.

Key words: galaxies: clusters: individual (Abell 160) – galaxies: evolution – galaxies: general – galaxies: ISM – galaxies: kinematics and dynamics

1. Introduction

The evolution of galaxies is driven by physical mechanisms of either internal or external nature. Among the internal ones are the processes related to stellar evolution (e.g., star formation activity, Kennicutt 1998; Kennicutt & Evans 2012; Madau & Dickinson 2014; supernova explosions, Burrows 2000; France et al. 2010; Marasco et al. 2015; Fielding et al. 2017), nuclear activity (accretion on a supermassive black hole and the related release of mechanical energy, Silk & Rees 1998; Fabian et al. 2003; Croton et al. 2006; McNamara & Nulsen 2007), and to the whole structural configuration of the different components (e.g., angular momentum reconfiguration by stellar bars, Hohl 1971; Weinberg 1985; Debattista & Sellwood 2000; Athanassoula 2002; Martinez-Valpuesta et al. 2006). As for the external ones, interactions with galaxies, with the gravitational potential of large, massive structures (such as galaxy groups or clusters), and with the dense, hot gas of the intracluster medium (ICM) are among those playing a major role.

Several such environment-dependent processes have been identified and proposed to explain the different evolutive paths that galaxies in clusters follow with respect to isolated galaxies, both regarding their stellar content (or, equivalently, their star formation history) and their morphology. These include harassment (repeated high-velocity encounters with galaxies in the cluster; Moore et al. 1996), starvation/strangulation (the removal, during the cluster collapse, of the galactic gas halo which fuels the star formation; Larson et al. 1980; Balogh et al. 2000), ram pressure stripping (the removal of the interstellar gas by means of high-velocity interactions with the ICM; e.g., Gunn & Gott 1972; Takeda et al. 1984; Faltenbacher & Diemand 2006), thermal evaporation (Cowie & Songaila 1977), major and/or minor mergers (e.g., Toomre 1977; Tinsley & Larson 1979; Mihos & Hernquist 1994; Springel 2000), or tidal effects of the cluster as a whole (e.g., Byrd & Valtonen 1990; Valluri 1993).

As the star formation history of a galaxy crucially depends on the amount of gas available, processes removing, adding, or even perturbing the gas ultimately determine the evolution and fate of a galaxy, at least as far as the stellar content is concerned.

Evidences of abruptly interrupted star formation due to gas removal (e.g., Steinhauser et al. 2016) as well as of enhancement of star formation (Boselli & Gavazzi 2006) are found in the cluster galaxy population. The latter phenomenon, in particular, is believed to be caused by the early effect of the ram pressure of the hot ICM that compresses the gas of the galaxy providing the dynamical instabilities needed to kick-start a star formation event (see, e.g., Crowl & Kenney 2008;

Steinhauser et al. 2012; Ebeling et al. 2014; Bischko et al. 2015; Merluzzi et al. 2016).

A spectacular example of distorted morphologies due to gas losses is the so-called jellyfish galaxies. First dubbed as such by Smith et al. (2010b) to describe the appearance of the filaments and knots departing from the main body of the galaxy, these objects are mostly found in clusters both locally (see, e.g., Fumagalli et al. 2014; Abramson et al. 2016; Merluzzi et al. 2016) and at high redshift (e.g., Cortese et al. 2007; Ebeling et al. 2014; McPartland et al. 2016). The availability of new generation Integral Field Units (IFU), such as the Multi Unit Spectroscopic Explorer (MUSE) on 8 m class telescopes, has opened a new window to study the physical processes at play in these galaxies.

GASP[9] (GAs Stripping Phenomena in galaxies with MUSE) is an ESO large program (P.I. B. Poggianti) that uses the second-generation IFU MUSE mounted on the Nasmyth focus of the UT4 at the VLT to observe a sample of 124 low-redshift ($z = 0.04$–0.07) galaxies with evidence of disturbed morphology in optical images of clusters from the WINGS/OmegaWINGS project (Fasano et al. 2006; Gullieuszik et al. 2015). GASP was granted 120 hr of time spread over four semesters from Period 96 (2015 October), and the second half of the observational campaign is currently being performed.

The ultimate goal of this project is to take a step forward in the understanding of the processes that remove gas in galaxies, halting the ongoing star formation processes. To what extent is the environment playing a role in gas stripping? Where is this more efficient? Why is it occurring and by which mechanism (s)? These are the most urgent questions that this project tries to address. We refer the reader to Poggianti et al. (2017) for a more detailed presentation of the survey, its characteristics, and its goals.

In this work, we focus on JO36, a galaxy drawn from the GASP sample. In the first part of the paper, we present an updated and improved version of SINOPSIS, the spectrophotometric fitting code we adopt for the spectral analysis of the whole survey, and use MUSE data of this object as a test case to validate the code. To this aim, we perform a comparison between SINOPSIS and GANDALF (Sarzi et al. 2006), a similar code that has been widely used to interpret the kinematics of stars and gas in galaxies from IFU data.

In the second part of the paper, we use the outputs of SINOPSIS to characterize the properties and distribution of the stellar populations in the galaxy and give an interpretation of its observed characteristics in relation to its position and dynamical status within its host cluster. Exploiting archival data, we calculate the dust mass and use this to derive an estimate of the total gas mass, while X-ray observations are used to constrain the possible presence of an active galactic nucleus (AGN).

As in all papers of the GASP series, we will assume a standard ΛCDM cosmology, with $H_0 = 70$, $\Omega_M = 0.3$, and $\Omega_\Lambda = 0.7$. Similarly, stellar masses and star formation rates are calculated assuming a Chabrier (2003) initial mass function (IMF). An observed redshift of 0.04077 like that of the galaxy under investigation, in this cosmology, corresponds to a luminosity distance of 180.0 Mpc and to an angular scale of $0\farcs81$/kpc, which results in a physical spaxel size of about 160 pc/spaxel for MUSE.

[9] http://web.oapd.inaf.it/gasp/index.html

2. The Spectral Fitting Code

In this section, we summarize the main features of SINOPSIS and describe new implementations and improvements with respect to its older versions.

2.1. Modeling Details

SINOPSIS[10] (SImulatiNg OPtical Spectra wIth Stellar population models) is a spectrophotometric fitting code that reproduces the main features of galaxy spectra in the ultraviolet to near-infrared spectral range. Here we summarize the most important aspects of SINOPSIS. We refer the reader to previous papers describing in detail the code's approach, its main characteristics, and the reliability of its performance (Fritz et al. 2007, 2011). The reader who is not interested in the technical details can safely skip this section and go directly to Section 3.

SINOPSIS has its roots on the spectral fitting code used by Poggianti et al. (2001) to reproduce the stacked optical spectra of a sample of luminous infrared galaxies of different spectral types. Since then, it has been successfully applied to derive the physical properties (stellar mass, dust attenuation, star formation history, mean stellar ages, etc.) of galaxies in various samples (Dressler et al. 2009; Fritz et al. 2011; Guglielmo et al. 2015; Vulcani et al. 2015; Cheung et al. 2016; Paccagnella et al. 2016). The code has been validated both by fitting simulated spectra of galaxies (Fritz et al. 2007) and by comparison with the results from other data sets and models (Fritz et al. 2011). Nowadays, SINOPSIS has been used to fit several thousands of optical spectra.

A number of other codes that serve similar purposes and are commonly used to derive the properties of the stellar populations and extinction in galaxies from their optical spectra, including, e.g., STARLIGHT (Cid Fernandes et al. 2005), STECKMAP (Ocvirk et al. 2006), VESPA (Tojeiro et al. 2007), GOSSIP (Franzetti et al. 2008), ULySS (Koleva et al. 2009), POPSYNTH (MacArthur et al. 2009), FIREFLY (Wilkinson et al. 2015), and FIT3D (Sánchez et al. 2016; but this list is most likely incomplete), can be found in the literature. SINOPSIS shares similar features with some of these codes while including substantial improvements.

In order to reproduce an observed spectrum, the code calculates the average value of the observed flux in a predefined set of spectral bands (see Table 1 for the set used in the MUSE data analysis), accurately chosen for the lack of prominent spectral features such as emission and absorption lines, and the equivalent width values of significant lines (i.e., the hydrogen lines of the Balmer series, the calcium H and K lines, plus the [O II] 3727 Å line, if present within the observed wavelength range), both in emission and in absorption. It then compares them to the same features in a theoretical model, which is created as follows.

From a set of ∼200 mono-metallicity simple stellar population (SSP) spectra with ages spanning the range between 10^4 and 14×10^9 years, SINOPSIS creates a new set, with a reduced number of model spectra, by binning the models of the original grid with respect to the SSP's age. In this way, the number of theoretical spectra shrinks to only 12 for any given

[10] SINOPSIS is publicly available under the MIT open source licence and can be downloaded from http://www.irya.unam.mx/gente/j.fritz/JFhp/SINOPSIS.html.

Table 1
List of Photometric Windows, Defined by the Respective Lower and Upper Wavelengths, where the Continuum Flux is Calculated to Compare Observed and Model Spectrum

#	λ_{inf}	λ_{sup}
1	4600	4750
2	4845	4853
3	4858	4864
4	4870	4878
5	5040	5140
6	5210	5310
7	5400	5500
8	5650	5800
9	5955	6055
10	6150	6250
11	6400	6490
12	6620	6690
13	6820	6920
14	7110	7210

Table 2
Maximum and Minimum Values Allowed for the Extinction, Parametrized by the Color Excess $E(B-V)$ and the SFR as a Function of the SSP's Age (the Latter Expressed in Years)

Age	$E(B-V)_{min}$	$E(B-V)_{max}$	SFR_{min}	SFR_{max}
2×10^6	0.0	1.50	0.0	3
4×10^6	0.0	1.50	0.0	3
6.9×10^6	0.0	1.50	0.0	3
2×10^7	0.0	1.00	0.0	3
5.7×10^7	0.0	0.80	0.0	2
2×10^8	0.0	0.40	0.0	2
5.7×10^8	0.0	0.40	0.0	2
10^9	0.0	0.40	0.0	2
3×10^9	0.0	0.20	0.0	1
5.7×10^9	0.0	0.20	0.0	1
10^{10}	0.0	0.20	0.0	1
1.4×10^{10}	0.0	0.08	0.0	1

Note. Note that the upper values for the SFR are normalized to the oldest SSP.

metallicity value. The choice of age bins is made based on the presence and intensity of spectral features as a function of age (see Fritz et al. 2007 for more details).

Each of these spectra is multiplied by an appropriate guess value of the stellar mass, and then dust attenuation is applied before the spectra are summed together to yield the final model. The combination of parameters that minimizes the differences between the constraints in the observed and model spectra is randomly explored by means of a simulated annealing algorithm. The range of values within which the search is performed is given in Table 2. The large range of extinction values that we allow is mainly meant to give a high degree of flexibility to the code, making it able to deal with galaxies having even "extreme" properties, without the need for further tuning.

2.2. The Treatment of Dust Extinction

One of the distinctive features of SINOPSIS is that it makes it possible to allow for differential extinction as a function of stellar age. In this way, the code simulates a selective extinction effect (Calzetti et al. 1994), where the light emitted by the youngest stellar populations is most likely to be affected by the presence of dust, which is typically abundant in star-forming molecular complexes. Once a stellar population ages, it progressively gets rid of this interstellar medium envelope, either by means of supernova explosions, which will blow it away, or because of the proper motions of the star clusters, or by a combination of the two effects.

Dust is found in the interstellar medium and is well mixed with the stars. A proper treatment of its extinction effect on the starlight would require the use of radiative transfer models, which can fully take into account the 3D geometry of dust and stars, and their relative distribution (see, e.g., the review by Steinacker et al. 2013). This is prohibitive for two reasons: one is the computational effort required to calculate such kinds of models, and the second is the lack of a detailed enough knowledge of the spatial distribution of these two components in any given galaxy.

Just like many other spectral fitting codes, SINOPSIS includes the effect of dust extinction by modeling it as a uniform dust layer in front of the source. Although this is indeed a simplification, Liu et al. (2013) have shown that a foreground dust screen reproduces well the effects of dust on starlight at large scales. Furthermore, the mix of stellar ages and extinction can be naturally taken into account by the age-dependent way of treating the dust attenuation allowed by SINOPSIS.

Different extinction and attenuation laws can be chosen including, among others, the attenuation law from Calzetti et al. (1994), the average Milky Way extinction curve (Cardelli et al. 1989), or the Small and Large Magellanic Clouds curves (Fitzpatrick 1986). Throughout this work and in all of the papers of the GASP series, we adopt the Milky Way extinction curve ($R_V = 3.1$).

2.3. Spectral Lines

Another key feature of SINOPSIS is the use of SSP models for which we have calculated the effect of nebular gas emission. Other models in the literature combine the effect of stellar and nebular emission, including, e.g., the works by Gutkin et al. (2016), Byler et al. (2017; but see also the pioneering work of Charlot & Longhetti 2001), who present models with both components, and Pacifici et al. (2012) and Chevallard & Charlot (2016), who describe an application of such kind of model to observed data.

SINOPSIS has had nebular emission lines included since its very first version (Poggianti et al. 2001, but see also Berta et al. 2003 and Fritz et al. 2007); these now have been recalculated for the new SSP models.

Including nebular emission lines in SSP spectra is a great advantage for a number of reasons: emission lines in the observed spectra do not need to be masked for the fitting, a reliable value for dust extinction can be calculated (even when Hβ is not observed), and star formation rates can be automatically estimated as well. Last but not least, especially for the purposes of the GASP project, correction of the underlying absorption in Balmer lines is performed in a self-consistent way by simultaneously taking into account both the absorption and emission components.

The calculation of the line intensities is obtained by preprocessing the SSP's spectral energy distribution (SED) with ages $\leqslant 5 \times 10^7$ years through the photoionization code CLOUDY (Ferland 1993; Ferland et al. 1998, 2013). The

Table 3
List of Spectral Emission and Absorption Lines that are Used, when Available, to Constrain the Model's Parameters

#	Line	λ_c
1	[O II]	3727
2	CaK	3933.6
3	CaH+Hϵ	3969
4	Hδ	4101.7
5	Hγ	4340.5
6	*Hβ	4861.3
7	*Hα	6562.8

Note. Lines indicated with an "$*$" are the ones contained within the wavelength range sampled by MUSE and are hence the only ones we use in this work and in all of the papers from the GASP series.

adopted parameters are those typical of an H II region (see also Charlot & Longhetti 2001): hydrogen average density of 10^2 atoms cm^{-3}, a gas cloud with an inner radius of 10^{-2} pc, and a metal abundance corresponding to the metallicity of the relative SSP.

Note that only SSPs with ages less than 2×10^7 years have a strong enough UV continuum to produce detectable emission lines and are, hence, the only ones for which gas emission is included.

The luminosity in the following hydrogen line series is computed: Balmer (from Hα to Hϵ), Paschen (from Paα to Paδ), Brackett (from Brα to Brδ), and Lyman (Lyα and Lyβ). The luminosity of UV and optical forbidden lines from various other elements (such as [O I], [O II], and [O III], [N II], [S II], and [S III]) is calculated as well. The latter are not used as constraints in the fitting procedure, as their intensities are dependent on several physical parameters (such as gas metallicity, geometry, electron temperature, electron density, ionization source, and dust depletion) whose determination is, at the moment, well beyond the scope of SINOPSIS.

Table 3 reports the list of spectral lines that are used as constraints in the spectral fits. The choice of the lines to be reproduced by the model is dictated mostly by the availability of a good physical characterization and understanding of the physical processes driving their intensities. This is why forbidden lines are not included, with the exception of the [O II] doublet at 3726, 3729 Å. Other absorption lines, such as the NaD doublet at 5890, 5896 Å, and the Mg line at 5177 Å, have a strong dependence on the α enhancement (e.g., Wallerstein 1962; Thomas et al. 1999) and on the presence of dust (this is the case with the sodium doublet; see e.g., Poznanski et al. 2012). As these features are not included in the theoretical models, we do not attempt to reproduce them.

On the other hand, the intensity of the [O II] doublet was found to correlate with the intensity of Hα (e.g., Moustakas et al. 2006; Weiner et al. 2007; Hayashi et al. 2013 for studies at various redshifts), such that the former is often used to quantify the SFR in distant galaxies, where Hα falls out of the observed spectral range. This is why the [O II] line is used as well.

The observed intensity of hydrogen emission lines, particularly those found in the optical range, are widely exploited to calculate the recent star formation rate and the amount of dust extinction. Hence, reproducing these observables with a theoretical spectrum gives strong constraints on these two quantities. For this reason, as a sanity check, we calculated the luminosity of the Hα line from our CLOUDY modeling, corresponding to a constant star formation rate over 10^7 years and checked that this value is consistent with the factor typically used to convert a Hα luminosity into a star formation rate value. We found a good agreement when considering a Chabrier (2003) IMF (see Kennicutt & Evans 2012 for a recalibration of this SFR indicator), as it is the case for the SSP version (discussed below) currently implemented in SINOPSIS.

As for the dust extinction calculations, the ratio between the observed intensities of the Hα and Hβ lines is commonly used, exploiting the fact that, in normal star-forming and H II regions, its theoretical expected value is $\sim$2.86 (see, e.g., Osterbrock & Ferland 2006). Indeed, the ratio of the luminosities of the two lines we calculated in spectra of various ages is 2.88, which is very close to the aforementioned theoretical value.

2.4. Recovered Parameters and Uncertainties

As we fully embrace the selective extinction hypothesis, the parameter space that SINOPSIS explores includes 12 values for the SFR and 12 values for the dust extinction, one for each age bin we consider. As extensively explained by Cid Fernandes (2007), using an over-dimensioned parameter space is an expression of the principle of maximum ignorance, and when the results are to be taken into account, the properties calculated over the initial 12 age bins must be compressed to a lower time resolution SFH. This, in our case, results in considering as a reliable result the SFR calculated in four time intervals (see below) and the extinction in two, namely "young" (i.e., for SSPs displaying emission lines) and "global" (i.e., calculated as an average over all the stellar ages).

The use of this nonparametric approach compared to, e.g., the assumption of an analytic prescription for the SFH (such as a tau-model, a log-normal, or a declining exponential), has the obvious advantage of limiting the number of priors the model needs to assume. Furthermore, it is a fairer representation of the stellar population evolution, the SFH of galaxies being in general characterized by various episodes of star formation of different intensities at various ages, especially when galaxies in dense environments are considered (see, e.g., Boselli et al. 2016).

Reconstructing the evolution of the stellar populations in a galaxy, by means of a nonparametric SFH as we do here, is a methodology that is by all means very similar to that embraced by other codes and works by tackling similar issues (see, e.g., Ocvirk et al. 2006; Merluzzi et al. 2013, 2016), and has proven effective for this task.

The choice of the number of age bins and their definition is based on simulations we have performed in Fritz et al. (2007) for integrated spectra of the WINGS survey. While, on the one hand, the quality of the spectra, especially in terms of the signal-to-noise ratio (S/N), is much better for MUSE data, on the other hand these spectra are sampling the rest-frame spectral region between $\sim$4700 and $\sim$9000 Å, and hence are missing some of those features normally used to constrain the stellar population properties. This is why we decided not to push our interpretation to a higher age resolution, despite the excellent quality of the data. However, we are still satisfied by the modeling and the provided results, since it is extremely difficult to disentangle the contribution to the integrated light of stellar populations in the 7–14 Gyr range. This is especially true when nonresolved spectroscopy is used, where in one single spectrum, stars of all possible ages are superimposed. Furthermore, well-known effects such as the age–metallicity

degeneracy plus dust extinction, conspire to make the spectra of simple stellar populations very similar in this age range.

Another viable approach would be to use an analytical prescription for the SFH (such as a log-normal, a double exponential, or a so-called τ-model), which is equivalent to imposing an arbitrary prior on the shape of the SFR as a function of time. This is why we choose to follow this "free" approach, which we consider fairer with respect to the complexity of the problem.

The derived physical parameters include the total stellar mass, SFR in the four age bins, luminosity and mass-weighted ages, and dust extinction (see Fritz et al. 2011 for a complete list). The latter is calculated as the ratio between the dust-free and the best-fit model, as explained in Fritz et al. (2011; see their Equation (6)).

The estimation of uncertainties in the physical parameters that are given as outputs, follows a Monte Carlo-like approach, described in detail in Fritz et al. (2007). The best fit is searched for within the parameter space by randomly exploring a large number of models. As the choice of the trial point (which hence results in a given model spectrum) performed at each step depends on the model calculated at the previous step, starting from a different set of initial conditions will always result in a different set of best-fit parameters (with minimal differences between best fits). The properties of the different best-fit models are hence used to calculate the uncertainties on the physical parameters.

2.5. Improvements and Adjustments for IFU Data Dealing

In order for SINOPSIS to properly deal with IFU datacubes, a number of changes and improvements were implemented with respect to the versions presented in Fritz et al. (2007, 2011). These are very briefly described below.

1. SINOPSIS can now ingest observed spectra in FITS format. Data format can be either 1D (a single spectrum), 2D (a series of spectra, as, e.g., provided by multislit or fiber-fed spectrographs), or 3D (e.g., an IFU, such as MUSE).
2. When data in "cube" format are used, most of the results are now saved on datacubes in FITS format, with each plane containing one of the properties typically derived from this kind of analysis (e.g., pixel-by-pixel stellar mass, extinction, star formation rate, stellar age, etc. See Fritz et al. 2011 for a detailed description of the meaning of each parameter).
3. A new set of SSP models by S. Charlot & G. Bruzual (2018, in preparation) is used, which has a higher spectral and age resolution, and a larger number of metallicity values (namely 13, from $Z = 0.0001$ to $Z = 0.04$, as compared to the three default values used before). These new models include the most recent version of the PADOVA evolutionary tracks from Bressan et al. (2012; PARSEC), and have been coupled with stellar atmosphere libraries from several sources depending on the wavelength coverage, luminosity, and effective temperature (see Gutkin et al. 2016 for the full compilation of the adopted stellar spectra). For the wavelength range of interest for this paper and for GASP in general, the stellar spectra are mostly from the Miles stellar library (Sánchez-Blázquez et al. 2006; Falcón-Barroso et al. 2011). The evolutionary tracks include the treatment of the Wolf–Rayet phase for stars typically more massive than 25 $M_{\odot}$. The assumed IMF is Chabrier (2003) with masses in the range 0.1–100 $M_{\odot}$.
4. One of the outputs now includes purely stellar emission, that is, the model spectrum without the nebular emission-line component. These are calculated from the best-fit parameters but using instead the SSP set with pure stellar emission.
5. When spectra from different regions of a galaxy are considered, it is possible that the velocities of the gas and of the stars are different. For our purposes, this means that during the spectral fitting, when using redshifts calculated from absorption lines (i.e., that of the stellar component), the center of the emission lines could be displaced with respect to the absorption component. This might turn into a miscalculation of the equivalent width of the lines or sometimes even to a nondetection. To overcome this possible issue, we now allow the simultaneous use of redshifts calculated from the two components. If no emission lines are detected, only the stellar redshift is used, while if emission lines are present, the measurement of the equivalent width is performed using the emission-line redshift for the lines in emission.
6. SINOPSIS has been optimized from the computational efficiency point of view and can successfully reproduce one optical spectrum in less than 1 s on a 3.5 GHz Intel Core i7 machine (running Mac OS X Version 10.10.5). The code is currently not parallelized and can only use one core at the time. We are planning to implement multithreading to exploit the full resource power of multicore computers for the analysis of multiple spectra/IFU data, which has proven to be quite computationally demanding.

3. Data

As already outlined in the introduction, this work provides a detailed analysis of a single galaxy drawn from the GASP sample. JO36 was selected from the sample of jellyfish candidates of Poggianti et al. (2016) found in the OmegaWINGS database (Gullieuszik et al. 2015). Also known as 2MFGC00903, or WINGS J011259.41+153529.5, this galaxy was chosen for testing and validating SINOPSIS because its SED is dominated by the emission of the stellar populations as opposed to the nebular one. In Figure 1, we present a g–r–z color composite image of the field where the galaxy is located and of the galaxy itself as derived from the MUSE cube.

JO36 (R.A. $= 01^{h}12^{m}59^{s}.4$; decl. $= +15^{d}35^{m}29^{s}$) is a disturbed galaxy with an assigned stripping class value JClass = 3 (on a scale of 1–5, where 5 represents the maximum morphological disturbance in the optical; see Poggianti et al. 2016) belonging to the Abell cluster A160. With a V-band magnitude of 15.5, JO36 is located at a projected radial distance of about 310 kpc from the Brightest Cluster Galaxy (BCG) and was recognized in optical images because of the presence of a bright optical tail, both in the V and B bands, departing from the galaxy disk toward the south. MUSE data for this object were taken in 2015 October 10, with an exposure of 2700 s.

The galaxy is classified as an Sc spiral seen almost edge on: its apparent axial ratio of about 0.15 is in fact consistent with the intrinsic flattening value usually assumed for galaxies with such a morphological classification.

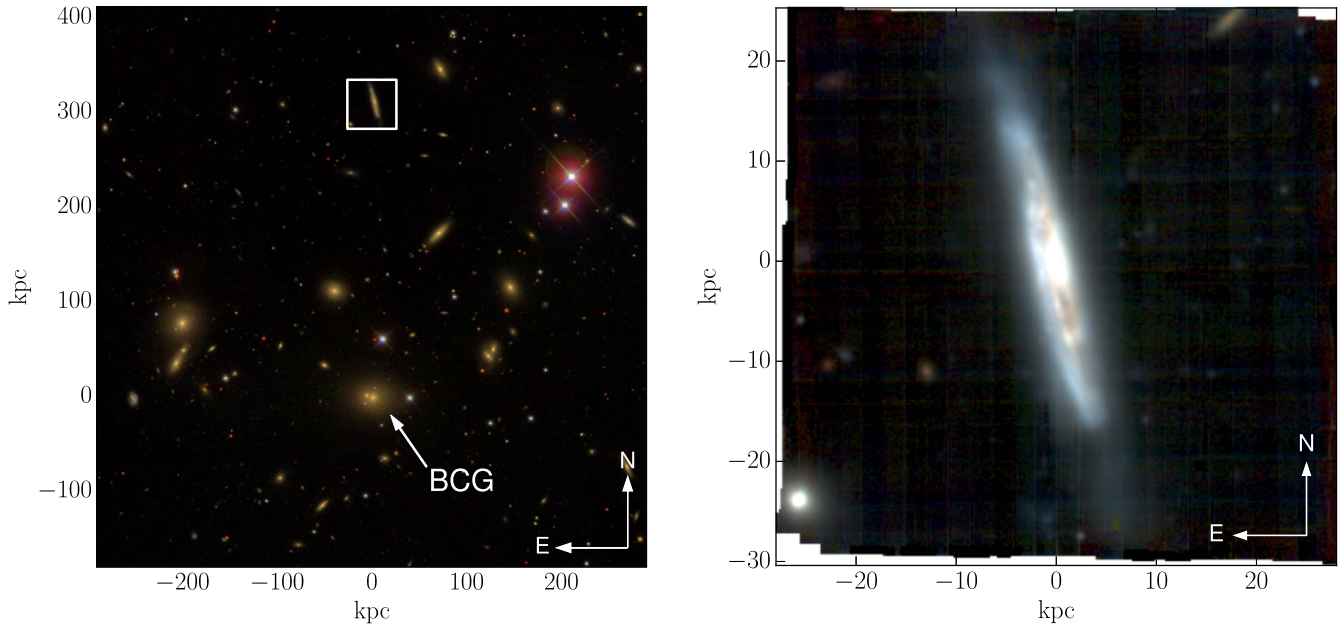

Figure 1. Left panel: SDSS color image of the central region of the cluster Abell 160 with the position of the BCG indicated, and the MUSE field of view around the galaxy. Right panel: RGB image of JO36, as provided by the MUSE data reduction pipeline. This is based on the *grz* bands, where the *g* filter is included at a 50% level due to the incomplete spectral coverage.

A bulge can be identified both photometrically and kinematically. The surface brightness profile, which we report in Figure 2, shows the bulge component as a light excess with respect to the exponential profile representing the disk (red line in the figure). As clearly visible in the plot, the bulge becomes dominant in the innermost 4 kpc. Similarly, the highest values of the stellar velocity dispersion are found in the central regions at similar galactocentric distances.

The data reduction for the whole GASP project is described in the survey's presentation paper, Poggianti et al. (2017), and we refer the reader to this work for all of the relevant details.

4. Comparison with GANDALF

We now briefly describe the main differences between SINOPSIS and GANDALF, by Sarzi et al. (2006), a code that is commonly used to perform a similar analysis on IFU data (see, e.g., Bacon et al. 2001; de Zeeuw et al. 2002, and other papers of the SAURON survey). We then compare the performances of the two codes, with a focus on the aspect that is the main driver of the comparison: the derivation of an emission-line-free model. This is done by analyzing the very same data set with both codes.

4.1. Differences Between the Two Codes

The choice of a comparison with GANDALF over many other similar codes is dictated by the need of subtracting, for a major part of the analysis of galaxies in GASP, the stellar component from the nebular lines when performing spatially resolved analysis on the gas properties. GANDALF is one of the most used tools to perform such a subtraction and was hence chosen as a reference.

As already outlined in Section 2.1, SINOPSIS has been used to analyze spectra from different instruments and various surveys. Still, an application to integral field data has so far been missing. Even though, in principle, it all comes down to correctly reproducing the most significant features of an optical

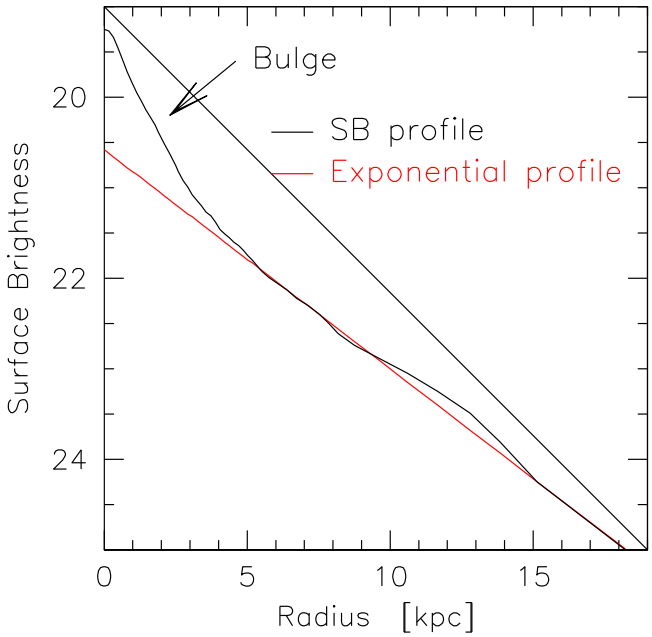

Figure 2. Surface brightness profile of the galaxy (black line), highlighting the presence of light excess, with respect to an exponential profile (red line), in the central regions. This is what we identify as the bulge.

spectrum, we performed a number of tests to check the reliability of the results when dealing with spatially resolved data. This was done by comparing our outcomes to those obtained with GANDALF, an IDL tool that shares similar features with SINOPSIS, but that focuses mostly on the analysis and interpretation of the emission and absorption line characteristics to derive the stellar and gas kinematics, even though the stellar population properties can be inferred as well.

Both codes attempt to reproduce, by means of theoretical spectra, the observed features of an optical spectrum. The underlying models are very similar, as they both use stellar

atmosphere from MILES (Vazdekis et al. 2010 for GANDALF and the similar version of Sánchez-Blázquez et al. (2006) for SINOPSIS), at a spectral resolution of ∼2.5 Å. They both provide an emission-line-free model spectrum.

The main differences between the two codes can be summarized as follows.

1. The models used by SINOPSIS already include the nebular emission, which has been self-consistently calculated using the SSP spectra as an input source fed into the photoionization code CLOUDY. GANDALF, instead, reproduces them as Gaussian functions, fitting not only their intensity, but their width and central wavelengths as well.
2. SINOPSIS assumes an extinction curve (either from models or derived from observations) to account for dust reddening in the models before matching to the observed ones, while GANDALF corrects for the effect of dust by multiplying the model spectra by nth-order Legendre polynomials.
3. SINOPSIS adopts a "selective extinction" approach, where the amount of dust attenuation is considered to be age dependent.

4.2. Direct Comparison

We ran the two fitting tools on a subset of pixels of the original MUSE cube, specifically on a rectangle of 109 × 255 spaxels which encompasses the full disk of the galaxy, and where a redshift value, either stellar or from the gas, was available (see also Section 5). Furthermore, we limited the wavelength range to the spectral window between 4750 and ∼7650 Å, discarding the red end of the spectrum, which is much less rich in the kind of features that are crucial for the purposes of this study.

We analyzed the performances of the two codes by calculating, a posteriori, the goodness of the fit to the continuum emission, hence not taking into account any spectral line (a further check is done on the equivalent width values of the Hα and Hβ lines in a separate comparison). To do so, we exploited the same 14 spectral windows used to constrain the fit for SINOPSIS. These windows have, in general, a width of ∼100 Å, except in a few cases in which they are narrower due to the need to sample a specific continuum emission region, while at the same time avoiding nearby emission or absorption features. The windows were chosen in order to homogeneously sample the whole spectral range (see Table 1 for the details).

For both codes, we calculated a goodness index, Γ, both "global" and for each of the aforementioned bands, defined as

$$\Gamma = \sum_{j=1}^{N} \Gamma^j = \sum_{j=1}^{N} \left(\frac{F_o^j - F_m^j}{\sigma^j} \right)^2, \quad (1)$$

where F_o^j and F_m^j are the average fluxes calculated over the jth band of the observed and model spectrum, respectively. σ^j is the uncertainty on the observed flux in that band, calculated as the standard deviation of the flux. Hence, Γ^j is the goodness index for the jth band. Note that, with the definition of the flux error bars we have chosen, we might be slightly overestimating the uncertainties on the flux in the highest S/N spectra. This is, however, irrelevant for the relative comparison as the errors are the same when the Γ index is calculated for SINOPSIS and GANDALF. In principle, one would expect that values of Γ^j lower than 1 (that is, with the model flux being within 1σ from the observed one) are to be considered acceptable fits. In reality, the values are always much smaller in the vast majority of the cases.

We constructed maps of both the Γ and Γ^j values for each of the 14 bands, so that we can check for the presence of systematic differences in any of the spectral ranges defined above.

The value of the goodness index, averaged over all of the spaxels, was found to be 0.85 and 1.37 in the case of SINOPSIS and GANDALF, respectively, indicating that the two codes provide, globally and on average, very satisfying fits to the observed data, with SINOPSIS performing slightly better than GANDALF.

We note that, in order for SINOPSIS to provide satisfactory fits, in particular toward the bulge of the galaxy, we needed to relax the constraints on the maximum values of dust extinction, in particular for the oldest stellar populations. In SINOPSIS, this parameter is allowed to vary freely with stellar age, as explained in Section 2.2. Normally, the upper limits of the values that dust extinction can reach for each stellar population are an inverse function of their age. This can be viewed on an equal footing with a prior that helps limit the effect of possible degeneracies.

The maximum value of the color excess was increased to 0.6 for the two oldest stellar populations and to 0.8 for the others up to ∼50 Myr (see Table 2 for a comparison to the standard values).

Allowing older stars to be more heavily affected by dust extinction is not a mere matter of increasing the degree of freedom of the parameters, but has an actual physical meaning: the central part of the galaxy is the most crowded area, and the light emitted by old stars is easily contaminated both by other stellar populations with a whole range of stellar ages, and also by the presence of dust located anywhere along the line of sight. The orientation of the galaxy is, in fact, very far from being face on (see Section 3), a configuration that would minimize the dust reddening effect (see, e.g., De Looze et al. 2014). Hence, the light reaching us from the innermost part has a contribution from both the bulge and the disk, which is likely to contain the majority of the dust. Allowing higher values of dust extinction even for the older stars that are dominating the bulge is hence needed to account for the effect of the dust lane.

In Figure 3, we show the Γ map calculated as explained above for both codes (note that the values for each spaxel are calculated according to Equation (1), and hence not normalized to the total number of observables). A visual comparison of the two maps in Figure 3, where only pixels having a stellar redshift or an S/N > 5 for the Hα emission line are shown, confirms the aforementioned result, highlighting that SINOPSIS performs slightly better with respect to GANDALF, at least as far as the continuum emission is concerned.

It can be easily noted that the Γ values decrease, on average, as a function of the galactocentric distance for both models. This is due to the fact that the spectra become fainter as we approach the galaxy outskirts, and the S/N hence gets lower. This increases the observed uncertainties on the fluxes, and it

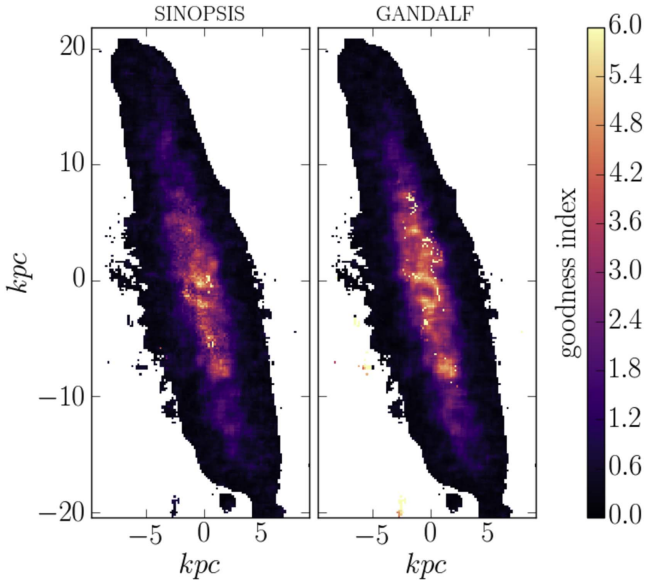

Figure 3. Maps of the goodness index (see Equation (1)) for SINOPSIS (left panel) and GANDALF (right panel), for the central spaxels (with pixel coordinates within the $106 < x < 217$ and $60 < y < 307$ range) of JO36, where the two codes were run for comparison. The values of Γ are displayed in a linear scale ranging from 0 to 6.

consequently makes the fits more degenerate, giving, as a result, lower values of the goodness index.

As for the other observed features, namely, the spectral lines, an automatic comparison with the data is much less straightforward, due to the complexity of properly measuring emission and absorption lines, especially in the lowest S/N spectra. Hence, we performed two quality checks: in the first one, we compared observed and model spectra, while in the second we focused on possible differences between the models provided by the two codes.

For the first one, we visually inspected the fits to the observed spectra provided by the two codes around the Hα and Hβ lines, checking for differences. This was done in a subset of $\sim$150 spaxels along the major and minor axes of the galaxy, which not only allowed the full range of S/N values found in the datacube (i.e., from $\sim$80 to $\sim$10) to be included, but also the different spectral properties, such as continuum shape and line intensities, to be sampled.

No significant differences were found between the two codes. On a minor fraction of the spectra in this control sample (less than 10%), SINOPSIS better recovers the Hβ emission, especially when deeply embedded within the absorption profile. In these cases, GANDALF was usually overestimating the emission-line intensity, but no systematic trend could be found, e.g., with respect to the S/N or to the spectral properties (also given the small number of spectra where this discrepancy was spotted).

In the second check, we calculated the equivalent widths of the Hα and Hβ lines from the best fits and compared the values from the two models. On average, we found a difference of about 15% in the value of the equivalent width of the two lines when comparing measurements in each spaxel. In Figure 4, we show the map of the spaxel-by-spaxel differences, expressed as a percentage of the Hβ equivalent width value (which is the feature displaying the largest difference), calculated as

$$\Delta_\beta = \frac{\mathrm{EW}_s - \mathrm{EW}_g}{\mathrm{EW}_s}, \quad (2)$$

where EW_s and EW_g are the equivalent width values, expressed in Å, of the SINOPSIS and GANDALF models, respectively.

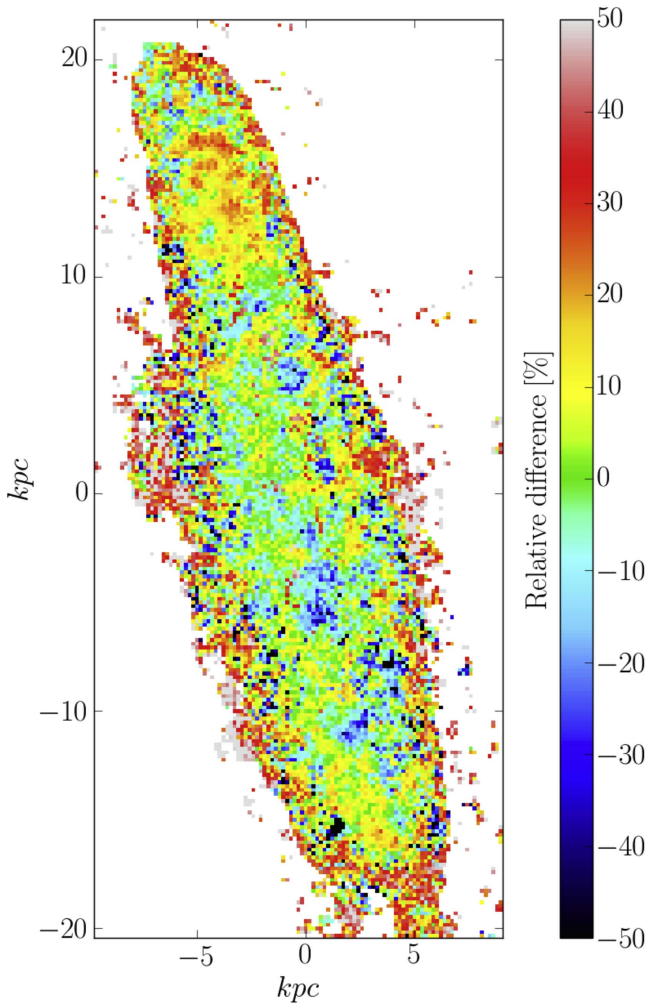

Figure 4. Map of the relative difference in the Hβ equivalent width values of the two models, calculated as in Equation (2), for each spaxel.

As shown in Figure 4, the differences are mostly within $\sim$5% across the galaxy, with very few exceptions where the discrepancy can be as high as $\sim$50%, but mostly in the outskirts of the disk, where the S/N is lower. We visually inspected the fits from both codes for a sample of these spaxels with the highest discrepancies and found that differences in the line intensities are either due to the high uncertainties in the measurement or, in many other cases, to GANDALF, which seems to display some issues fitting (or measuring) the observed line (e.g., because of a poor fit of the continuum emission near the line, which hence affects the line measurement itself).

We conclude that the two codes perform, with respect to the determination of the spectral continuum emission and of the hydrogen absorption line intensity, very similarly. This gives us strong confidence in the model fits provided by SINOPSIS, in particular with respect to the correction of the absorption component in the Balmer lines, which was our major interest.

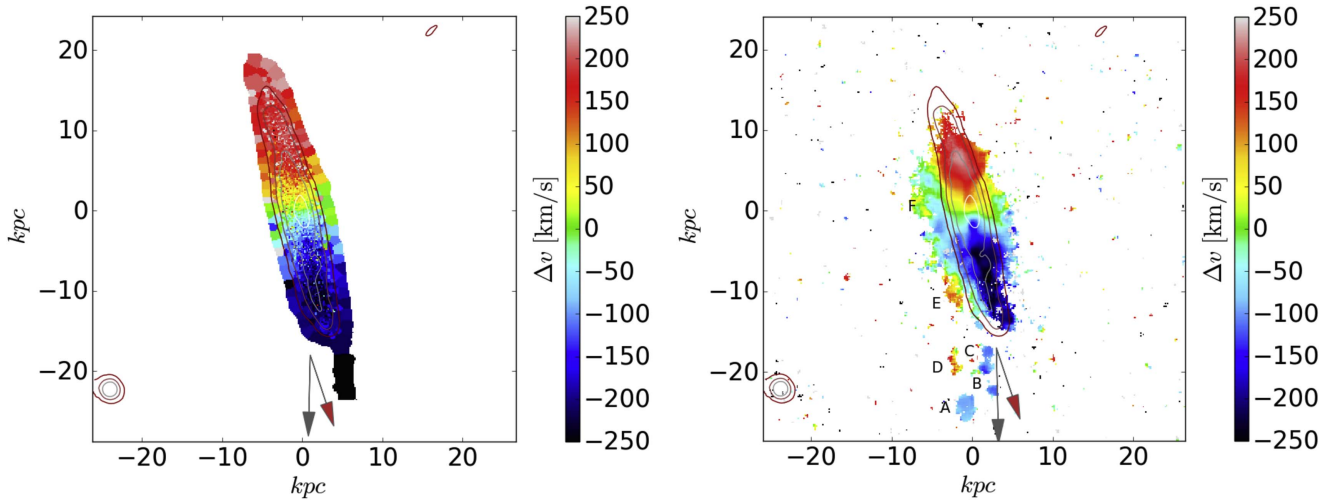

Figure 5. Left panel: stellar velocity map. Right panel: gas velocity map. The solid lines in both figures are the Hα continuum surface brightness contours in four logarithmically spaced levels. Regions labeled "A" to "F" are described in the text. The gray and red arrows point toward the BCG and the cluster X-ray emission, respectively. A cut of 4 in S/N was applied in the gas velocity map. North is up, east is left.

5. Results

We now present the results of the kinematic and stellar population analysis. The stellar and gas velocities were derived by means of external packages. In particular, the fitting and characterization of the emission lines was performed by exploiting the KUBEVIZ (Fossati et al. 2016) code, while the stellar velocities were measured by the pPXF software (Cappellari & Emsellem 2004; Cappellari 2012), which works in Voronoi binned regions of a given S/N (10 in this case; see Cappellari & Copin 2012).

The gas and stellar velocity information is also used to assign a proper redshift, which will be used in the spectral fitting. Only spaxels with a redshift determination will be analyzed by SINOPSIS.

5.1. The Stellar and Gas Kinematics

The stellar kinematics was derived, as customary for this kind of data, from the analysis of the characteristics of absorption lines, while the kinematical properties of the gas were inferred from a similar analysis of the Hα emission line, using the aforementioned tools. We refer to Section 6.1 in Poggianti et al. (2017) for a detailed description of how the gas and stellar kinematics are derived from these tools and of the main parameters adopted for this task.

In Figure 5, we show the velocity map of the stellar and gas components, while Figure 6 presents the radial velocity profiles along the major axis for stars (red triangles) and gas (blue dashed line). At radii larger than ∼10 kpc, the trend becomes much noisier due to the fewer usable spaxels and to the more uncertain velocity determination. A cut at S/N = 4 measured on Hα was applied in the gas velocity map. In order to obtain more reliable gas velocities, the original datacube was filtered with a 5 × 5 spaxel boxcar filter to increase the S/N level.

Although following the same pattern in the velocity profiles, the gas has velocities that are marginally higher with respect to those measured in the stellar component, even though this difference is in most of the cases within the measured uncertainties (see Figure 6).

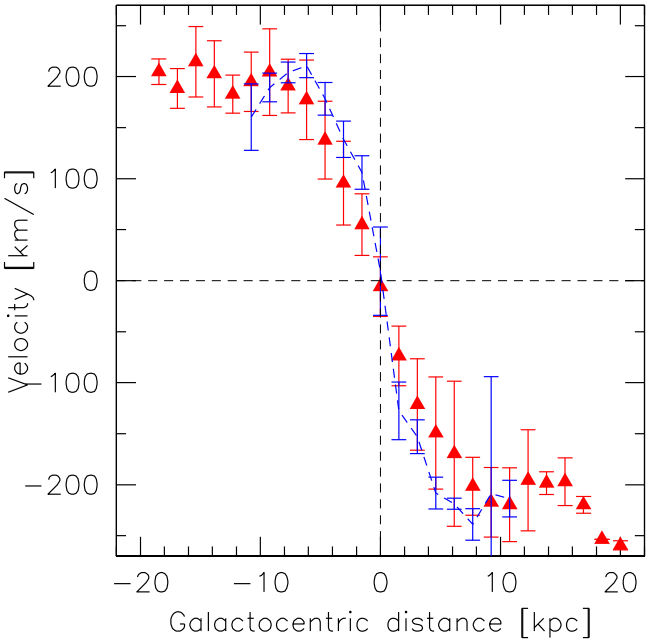

Figure 6. Stellar (red triangles) and gas (blue, dashed line) radial velocity profiles taken along the major axis of the galaxy.

The radial distribution of the stellar velocities displays a monotonic gradient out to radii of about 10 kpc, with values as high as ∼200 km s^{-1}, as expected from a nearly edge-on galaxy and is a clear indication of a rotationally supported disk. After this radius, the velocity gradient flattens out in the northern part of the disk while displaying a slight bump on the southern side, reaching higher velocities farther out. These velocities correspond to stars observed in a tail extending by about 5 kpc southwards, where the (stellar) radial velocities are the highest found in the disk, with (negative) values of about 270 km s^{-1}. This velocity pattern follows the trend observed in the inner disk, while the northern side shows no evidence of a similar structure, which is absent in both WINGS and OmegaWINGS images.

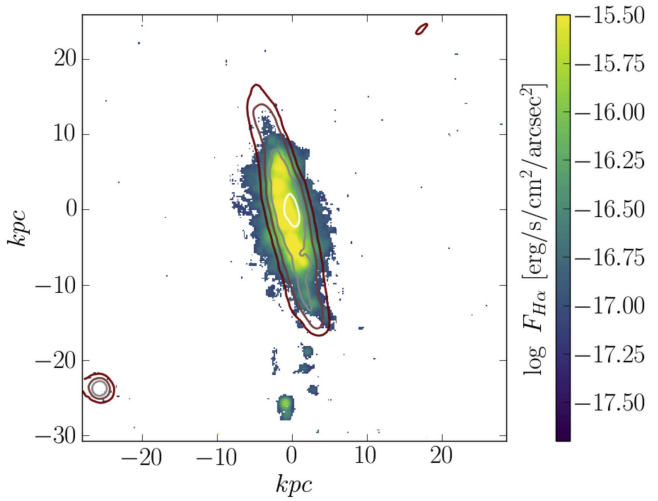

Figure 7. Hα surface brightness map. The red lines are the stellar emission isocontours derived from the Hα continuum emission.

The "rotational axis" of the gas component (i.e., the locus of close-to-zero velocities) visible in Figure 5 as a green strip is bent in a twisted "U" shape, with zero-velocity gas found in the outer disk, as far as ∼5 kpc away from the minor axis. Such a feature is similar to that observed by Merluzzi et al. (2016) in the jellyfish galaxy SOS90630 of the Shapley supercluster.

Using an ad hoc *N*-body/hydrodynamical simulation, they found that the gas velocity field, and this very feature in particular, can be successfully reproduced when ram pressure stripping is acting on an almost edge-on geometrical configuration (see their Figures 18 and 27), with the galaxy moving in the opposite direction with respect to the concavity.

A careful inspection of the gas velocity map highlights asymmetries in their values, with negative velocities extending well beyond the galaxy's center toward the north, out to a distance of about 8 kpc on the eastern side of the disk (see the region marked "F" in Figure 5). Similarly, on the same side but toward the south, there is a clear inversion in the gas velocities, going from negative to positive values (region "E" on the same figure).

Four Hα blobs are visible toward the south, detected with S/N from ∼10 (the regions labelled "B," "C," and "D") to more than 50 (region "A," the southernmost one). The most luminous one, region A, is clearly detected on the *V*-band image of WINGS and OmegaWINGS data as well. The velocities of blobs A, B, and C are quite compatible with those observed in the southern disk, while those in region D are similar to those of the northern side. A feature with similar velocities is found on the southeast side of the disk (labelled "E" in Figure 5), with counterrotating velocities with respect to the gas on this side of the galaxy.

5.2. The Spatially Resolved Gas Properties

The Hα surface brightness map is shown in Figure 7. The map reaches a surface brightness of 2×10^{-18} erg s^{-1} cm^{-2} arcsec^{-2} at the 3σ limit (which is the characteristic value for MUSE data of this program; see Poggianti et al. 2017) and, when compared to the stellar emission (see, e.g., the stellar velocity map), it shows evidence for the truncation of the ionized gas disk. Ionized gas is found out to galactocentric distances of about 15 kpc, while the stellar disk extends to ∼25 kpc (with a surface brightness detection limit in the *V* band of ∼27 mag arcsec^{-2} at the 3σ confidence level). In Section 7, we will discuss the possible origin of this truncation.

We created diagnostic diagrams (see, e.g., Kewley et al. 2006) using emission lines lying within the observed range of our data (i.e., Hβ [O III] 5007 Å, [O I] 6300 Å, Hα, [N II] 6583 Å, and [S II] 6716+6731 Å) to derive the characteristics of the ionizing sources as a function of the position and to detect the possible presence of an AGN. The line intensities were measured after subtraction of the continuum, exploiting the pure stellar emission best-fit model provided by SINOPSIS, in order to take into account any possible contamination from stellar photospheric absorption.

The three diagrams we used, namely, log[N II]/Hα versus log[O III]/Hβ (shown in Figure 8), log[O I]/Hα versus log [O III]/Hβ, and log[S II]/Hα versus log[O III]/Hβ (not presented in this paper), are concordant in excluding the presence of an AGN. We consider this result to be quite robust, given that in the center of the galaxy, where a possible AGN is likely to be located, the measured S/N is the highest.

Interestingly enough, deep *Chandra* archive images have detected the presence of a luminous though highly absorbed X-ray source strongly incompatible with a possible nuclear starburst, as described in Section 5.4 (and F. Nicastro et al. 2017, in preparation). This would imply that, if an AGN is indeed the source of this luminosity, it should be highly obscured so that it would not be detected by optical line diagnostics.

The results, presented in Figure 8, show that the emission-line luminosity is powered either by star formation or by LINER-like mechanisms such as shocks. In particular, the central parts of the disk are those dominated by star formation, while the gas at higher galactic altitudes shows characteristics of LINER emission or characteristics intermediate between the two (see the right panel of Figure 8).

Clear signatures of stripping along the line of sight are visible as double-peaked emission-line profile, or as a departure from a Gaussian profile, mostly visible in Hα. These are located in the outskirts of the disk, in regions with a LINER emission origin.

It is interesting to notice that the regions classified as "star-forming" in the left panel of Figure 8 are clearly displaced toward the east with respect to the center, defined by the Hα continuum contour, and slightly bent with respect to the major axis.

5.3. Properties of the Stellar Populations

We now study both the global and spatially resolved stellar populations of this galaxy by analyzing the SFR as a function of time in four age bins. These are logarithmically spaced and chosen in such a way that the differences between the spectral characteristics of the stellar populations are maximal and are defined according to Table 4.

The stellar population properties were obtained by applying SINOPSIS to the observed datacube in each spaxel with a reliable redshift determination, using three sets of SSP spectra with fixed metallicity values (namely, $Z = 0.004$, $Z = 0.02$, and $Z = 0.04$). Whenever a stellar redshift was available, this was used for the spectral fitting, while the equivalent widths of the emission lines were measured using the redshift value derived from the emission lines. About 15,000 observed spectra were analyzed (the runtime takes approximately 8 hr).

The total stellar mass, calculated as the sum of stellar masses in all of the spaxels encompassed by region 4 (the larger ellipse

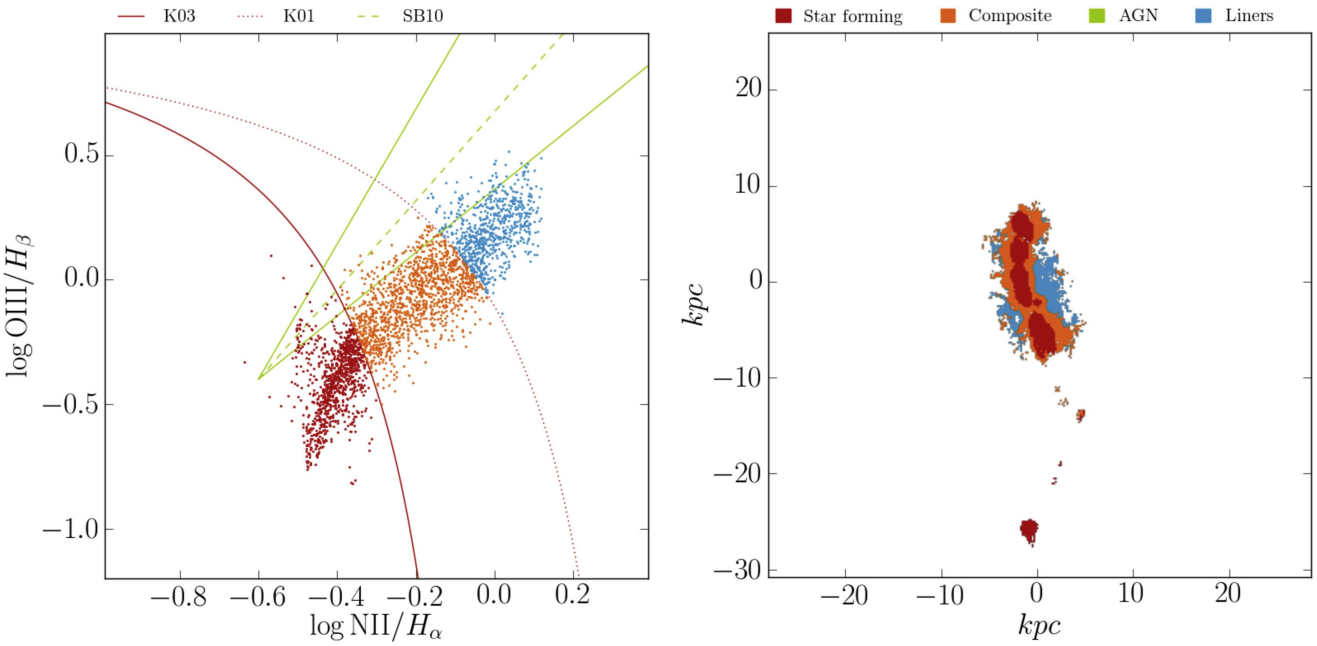

Figure 8. Left: diagnostic diagram of the ionizing sources across the galaxy. The red dotted and continuous lines are defined as in Kewley et al. (2001) and Kauffmann et al. (2003), respectively. The green lines are taken from Sharp & Bland-Hawthorn (2010; see the text for details.) Right: spatial locations of the spaxels color-coded based on the ionizing source diagnostic. Hα continuum surface brightness contours are shown as a reference for the stellar emission.

Table 4
Ages of the the Stellar Populations, in Years, for Which We Calculate the Physical Properties from the Spectral Fitting

Bin	Lower Age	Upper Age
1	0	2×10^7
2	2×10^7	5.72×10^8
3	5.72×10^8	5.75×10^9
4	5.75×10^9	14×10^9

in Figure 9; see also Table 5), is $6.49^{+0.16}_{-0.19} \times 10^{10}\,M_\odot$ and is slightly higher than $4.8 \pm 0.8 \times 10^{10}\,M_\odot$, which is the the mass value calculated from the WINGS integrated spectrum, after correcting for aperture effects.[11] Using SINOPSIS to derive the stellar mass from the integrated spectrum of region 4 yields a value of $5.89^{+0.89}_{-1.14} \times 10^{10}\,M_\odot$, which is fully compatible with the value calculated from the spatially resolved data.

Similarly to the stellar mass, SINOPSIS also provides an estimate of the recent (i.e., $\lesssim 2 \times 10^7$ year) SFR. This value is obtained by summing the SFR values in each spaxel, and it already contains a correction for dust extinction, which is performed within the spectral fitting procedure. The integrated value of the recent SFR calculated in this way is $5.88^{+1.57}_{-0.93}\,M_\odot\ \mathrm{yr}^{-1}$, about 90% of which is concentrated within the innermost parts, where the dust extinction also reaches the highest values as shown in Figure 15 (this corresponds to the spaxels enclosed within ellipse n.2 in Figure 9).

To find possible trends in the stellar properties as a function of the position, we considered four annuli, defined as the regions in between elliptical apertures, which are chosen to match roughly the surface brightness intensity of the stellar emission at different levels. These are depicted in Figure 9. Table 5 reports the physical sizes of the ellipses. Furthermore,

[11] The main source of error on this mass is probably due to the quite large aperture correction which, on top of that, is even more uncertain for edge-on galaxies.

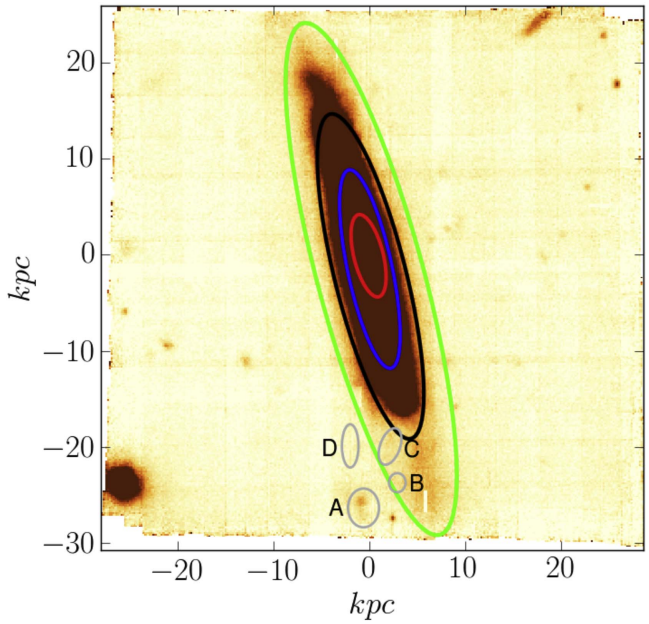

Figure 9. MUSE datacube integrated with respect to the wavelength. The ellipses are the areas where the SFR is computed, with the same color-coding as in Figure 10. The gray ellipses and circles on the southern part are the four Hα blobs as identified in Section 5.1.

Table 5
Size, in Kiloparsecs, of the Major (a) and Minor (b) Semiaxes of the Ellipses Defining the Regions in Figure 9

Region	*a*	*b*
1	4.1	1.4
2	9.8	2.2
3	16.2	3.5
4	25.6	5.1

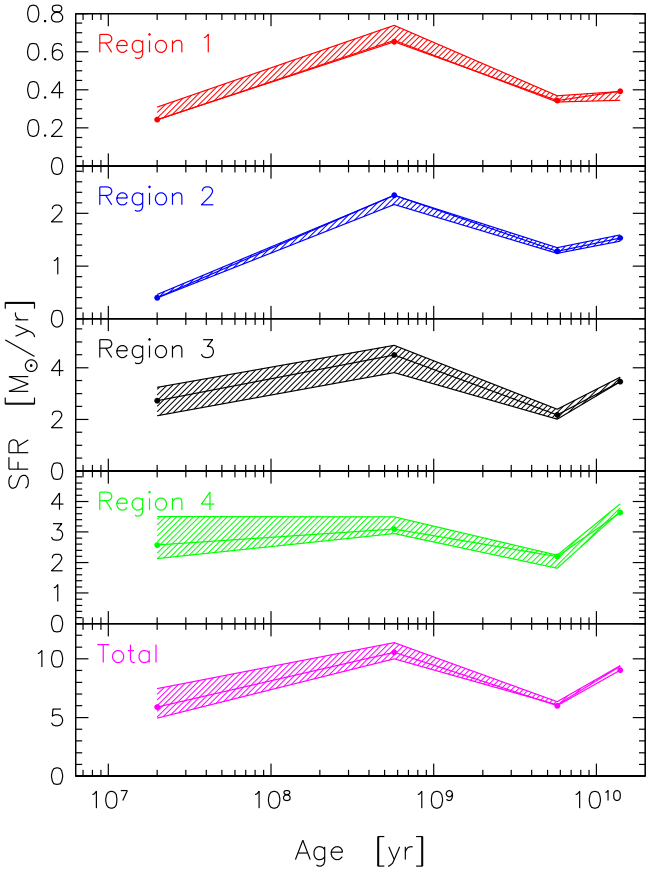

Figure 10. The first four panels from the top show the star formation history of the galaxy calculated within the annuli defined in Figure 9 (same color-coding) and Table 5. These are labelled from 1 to 4 going from the innermost to the outermost region. The lowest panel displays the same quantity but for the whole galaxy.

we separately analyze the star formation histories of both the stellar tail and the four Hα emission blobs identified in Figure 5.

Calculating the SFR in the previously defined annuli is an effective way to look for broad spatial trends in the average ages of the stellar populations as a function of the galacto-centric distance. After the first star formation episode, when about 65% of the stellar mass was created, the galaxy underwent a decrease in the star-forming activity, followed by a subsequent star formation episode with an intensity, relative to the previous age bin, higher in the outskirts with respect to the center.

This is clearly represented in Figure 10, where we show the SFR as a function of age and position. This is indicative of an inside-out formation scenario in the early epochs of the galaxy: the SFR decreased after the initial burst more abruptly in the innermost regions while being sustained at a higher rate in the disk outskirts. An intense star formation activity involving the whole galaxy occurred between 20 Myr and 0.5 Gyr ago, with a much higher intensity in the outer part than in the galaxy center. During this event, the SFR increased by only ∼15% in the innermost region (region 1), while the outer parts (regions 3 and 4) experienced a boost of almost 50%.

This event converted, according to our modeling, about 10^{10} $M_{\odot}$ of gas into stars in the outer disk (i.e., the annulus between ellipses 2 and 4), an amount that represents about 15% of the currently observed total stellar mass in the whole galaxy.

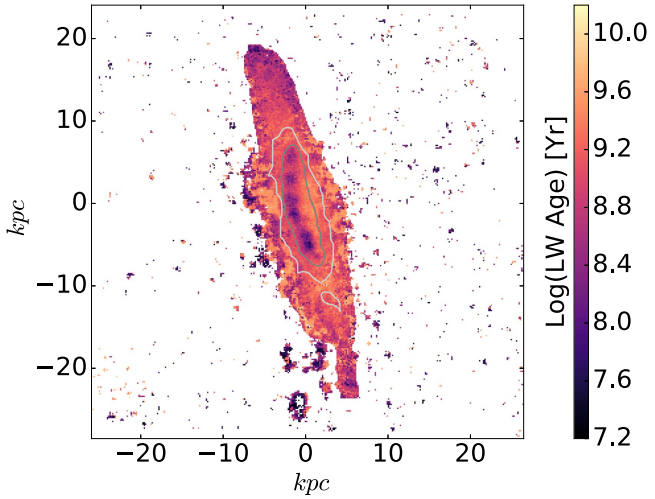

Figure 11. Map of the luminosity-weighted stellar age as calculated from spectral modeling.

The luminosity-weighted age map, shown in Figure 11, highlights the changes in the average age of the stellar populations at each location in the galaxy. This displays a minimum in the central parts of the galaxy, as expected given that it is at this location where bulk of the star formation is happening. Very young ages are found in the blobs located in the southern outskirts as well, which are all found to be star forming. This is consistent with the faint stellar continuum and Hα being observed in emission, and it is further backed up by the low value of the luminosity-weighted ages.

Figure 12 presents the spatially resolved star formation rate surface density in four age bins. These are calculated by rebinning the SFR values of the 12 SSPs used for the fit, according to the definition and ages given in Fritz et al. (2007).

There are no signs of ongoing star formation outside the disk, except for the southern blobs where we clearly detect ionized gas. Indeed, the top-left panel in Figure 12 shows that the most intense star-forming spaxels are found within the central parts of the disk with values up to $\sim 5 \times 10^{-2}\, M_{\odot}\, \mathrm{yr}^{-1}\, \mathrm{kpc}^{-1}$, while outside this region, very well defined by the Hα continuum contours, only very faint and sparse signatures of current star formation are found.

The outermost parts of the disk are dominated by intermediate-age (i.e., between $\sim 2 \times 10^7$ and $\sim 6 \times 10^8$ years) stellar populations; these very same stars are also the main population found in the tail departing from the southern disk that was identified in Figure 5, where no emission lines were detected. The oldest stars are dominating the bulge of the galaxy, and they are the most concentrated population as depicted in the lower-right panel of Figure 12.

In the most luminous blob "A," the Hα equivalent width reaches a value of −64 Å. The star formation rates derived from SINOPSIS from the integrated spectra of the blobs, range from 3×10^{-3} (blob B) to $1.2 \times 10^{-2}\, M_{\odot}\, \mathrm{yr}^{-1}$ (blob A), while the stellar masses have values in the range between 5.1×10^6 (blob D) and $1.7 \times 10^8\, M_{\odot}$ (blob A). Relatively young ($\lesssim$500 Myr) stars are present throughout the entire disk.

We point out that the spatial trends we observe in the stellar population properties are very likely weakened by projection effects, given the high inclination angle of the galaxy, and might be actually even stronger.

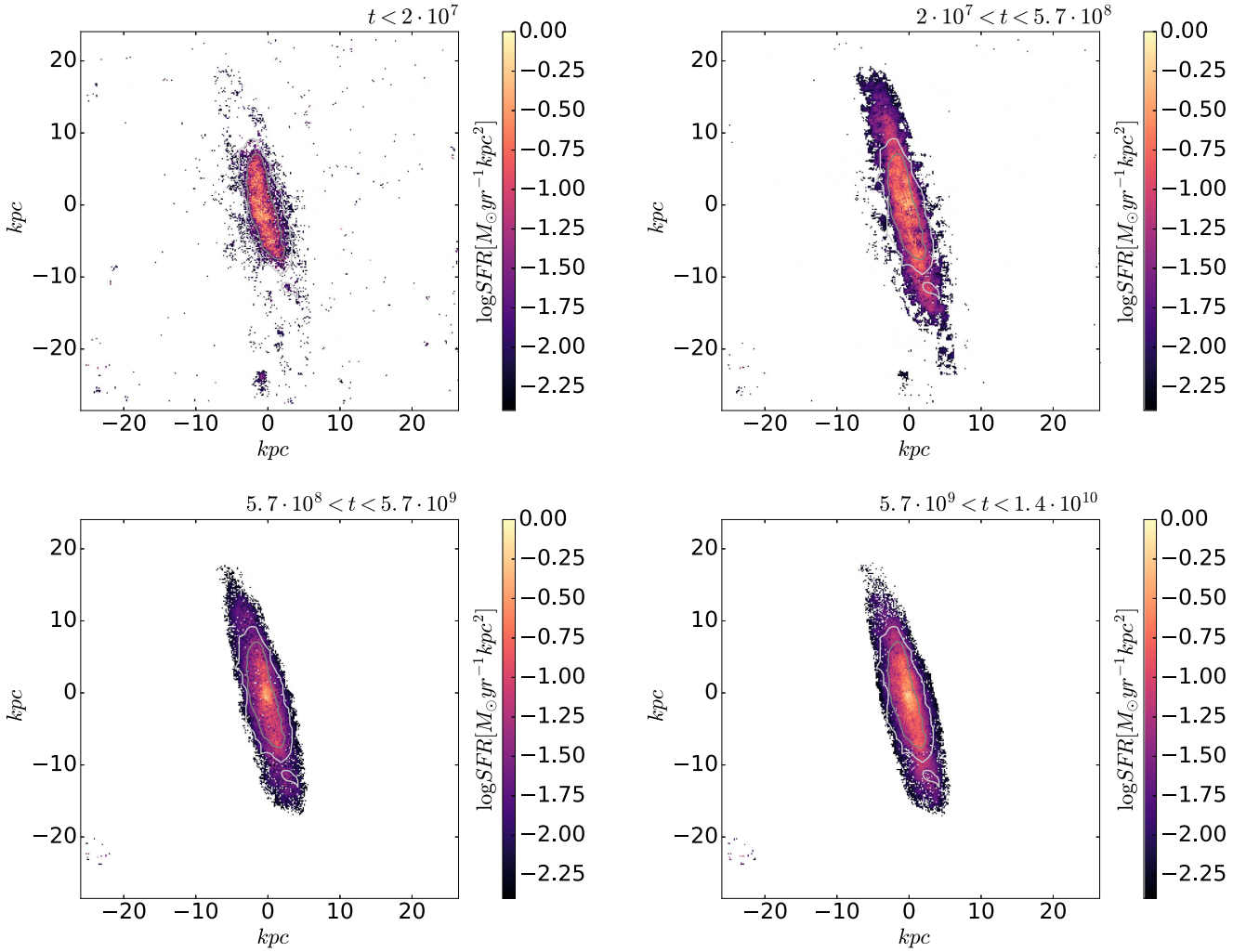

Figure 12. Star formation rate surface density as a function of position for different epochs corresponding to the four main SSP age bins. The contours are defined in the same manner as for Figure 5. The ring-like structure visible in the youngest stellar population is an artifact from the code, which mistakes noisy features for an Hα line in emission.

5.4. The Chandra View of the Nuclear Region of JO36

JO36 was serendipitously observed by *Chandra* on 2002 October 18 as part of the targeted observation of the cluster Abell 160 and for a total of 58.5 ks. The galaxy is located 5.8 arcmin off-axis, with respect to the *Chandra* ACIS-I aimpoint, where the 2 keV off-axis/on-axis effective area ratio (i.e., vignetting) is ∼0.9, and the Point Spread Function Encircled Energy Radius is ∼1.5–2 arcsec (cf. with ∼0.5 arcsec on-axis; "The *Chandra* Proposal Observatory Guide," v. 19.0, http://cxc.harvard.edu/proposer/POG/html/chap6.html).

A bright X-ray nucleus is clearly detected (Figure 13, left panel) at a position coincident with that of the bright Hα nucleus (Figure 13, right panel), together with several fainter point-like X-ray sources (most likely ultraluminous X-ray—ULX—sources; F. Nicastro et al. 2017, in preparation), aligned with the galaxy's edge-on disk seen in Hα (white contours superimposed on the X-ray image in the left panel of Figure 13). Interestingly, the brightest of these off-nuclear X-ray sources is located just at the northern edge of the truncated gas disk, where little or no Hα emission is seen.

To estimate the X-ray luminosity of the nucleus, we extracted source and background X-ray counts respectively from a 3 arcsec radius circular region centered on the source

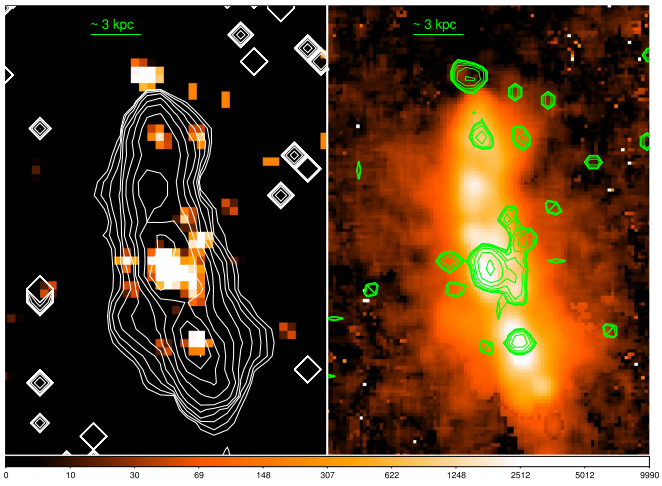

Figure 13. *Chandra* 0.3–10 keV (left panel) and MUSE Hα (right panel) images of the GASP cluster galaxy JO36: X-ray (green) and Hα (white) contours are superimposed on the Hα and X-ray images, respectively.

centroid (R.A. = 18.24788, decl. = 15.59122) and from four additional 3 arcsec radius source-free circular regions located ∼15 arcsec northeast and southeast of the nucleus. The nuclear

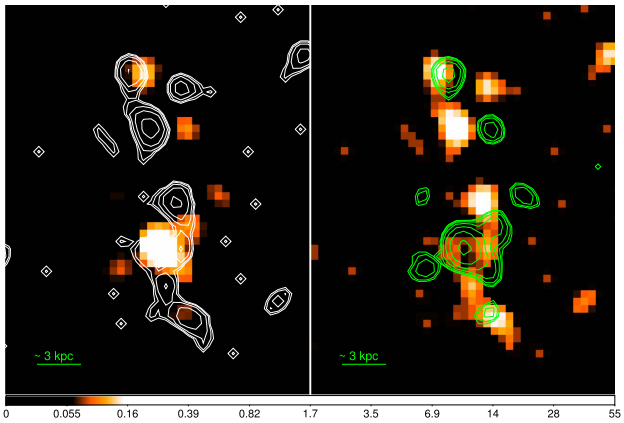

Figure 14. *Chandra* 2–10 keV (left) and 0.3–2 keV (right) images of the GASP cluster galaxy JO36.

region contains 32 full-band *Chandra* counts, while the four background regions contain a total of seven counts. Rescaling by the four times smaller source to background extraction area, this gives a net number of 0.3–10 keV source counts of 30.8 ± 5.6, or a count rate of $(5.3 \pm 1.0) \times 10^{-4}$ counts s^{-1}.

The nuclear X-ray counts are all detected above 2 keV (compare the left and right panels of Figure 14), which suggests that the X-ray emission is highly absorbed. Indeed, binning the ~31 source net counts into bins with $\geqslant$10 counts, leaves a three-bin spectrum ($E_{\rm bin} = 1.8$, 4.2 and 6.7 keV) peaked at 4.2 keV. Modeling the spectrum with a simple power law ($F = A(E/E_0)^{\Gamma}$) yields an extremely flat photon spectral index $\Gamma = -0.9$, which also underestimates the spectrum peak count rate. Including a column $N_{\rm H}$ of intrinsic nuclear cold gas surrounding the X-ray source, attenuating the soft X-rays along our line of sight, and freezing the photon spectral index to the commonly observed AGN value of $\Gamma = 2$ (e.g., Piconcelli et al. 2005) yields instead flat residuals and a best-fitting $N_{\rm H} = 1.1^{+0.7}_{-0.4} \times 10^{23}$ cm^{-2}, as typically observed in highly obscured type 2 Seyfert galaxies (e.g., Risaliti et al. 1999).

From the best-fitting spectral model, we derive an observed (i.e., absorbed) 2–10 keV flux $F_{2-10} = (3.5 \pm 1.5) \times 10^{-14}$ erg s^{-1} cm^{-2}, which translates (at the distance of JO36) into an observed luminosity $L_{2-10} = (1.4 \pm 0.6) \times 10^{41}$ erg s^{-1} and an intrinsic (i.e., unabsorbed) luminosity of $L^{\rm Unabs}_{2-10} = (2.8 \pm 1.1) \times 10^{41}$ erg s^{-1}. By factoring a bolometric correction factor of $\simeq$10 (appropriate for $L_{2-10} \simeq 3 \times 10^{41}$ erg s^{-1}; e.g., Marconi et al. 2004), we get $L_{\rm Bol} \simeq 4 \times 10^{42}$ erg s^{-1}, consistent with the low-luminosity end of Seyfert galaxies and thus pointing toward the presence of a buried AGN in the nucleus of JO36, which was not detected by optical diagnostic diagrams (Section 5.2).

An additional independent (but indirect) check of the presence of an AGN in the nucleus of JO36 can be done by comparing the star formation rate density (SFRD) derived in the nuclear region through Hα diagnostics ($\rm SFRD_{H\alpha} \simeq 0.14$ $M_\odot$ yr^{-1} kpc^{-2}), with the estimate derived by assuming that all 31 nuclear *Chandra* counts are uniformly distributed over a compact, $\lesssim$2.7 kpc (i.e., 3 arcsec) radius, nuclear starbursting region and are due to a large (i.e., $\gtrsim$100) number of unresolved luminous X-ray binaries. This gives an observed 2–10 keV luminosity density of $\mathcal{L}_{2-10} \gtrsim 7.6 \times 10^{39}$ ergs s^{-1} kpc^{-2}, which translates into an SFRD $\gtrsim 1.5\, M_\odot$ yr^{-1} kpc^{-2} (e.g., Ranalli et al. 2003). This is more than 15 times larger than that observed in Hα, again suggesting the presence of an AGN in the nucleus of JO36.

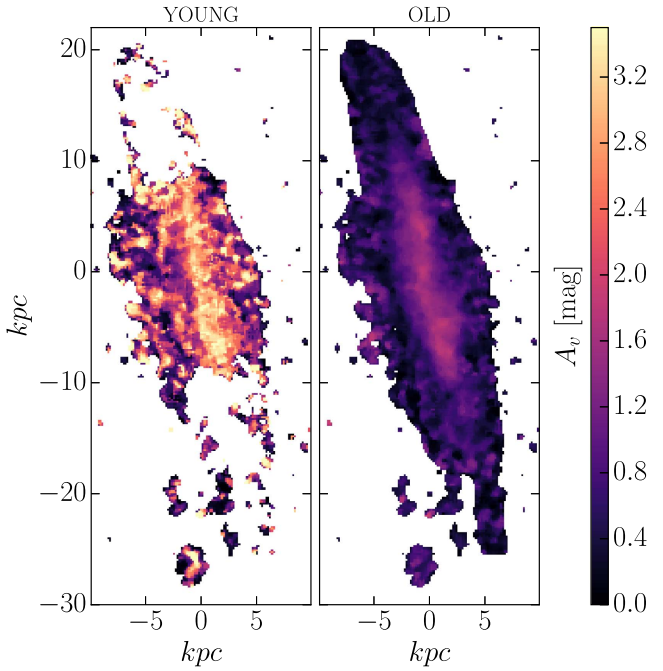

Figure 15. On the left panel, the extinction map for the youngest stellar populations (i.e., with age $\lesssim 2 \times 10^7$ years), as derived by spectral fitting, is presented. On the right panel, the same quantity is shown, but for older stars. Both maps were smoothed to improve readability.

6. The Interstellar Medium in JO36

SINOPSIS provides values for the emission-line dust attenuation, whose map we show in the left panel of Figure 15. A comparison with the same quantity calculated from the observed Balmer decrement (Hα/Hβ) shows excellent agreement. Values of A_V as high as 4 are found toward the central parts of the galaxy, this being partly due to the high inclination of the galaxy disk with respect to the line of sight.

In the right panel of Figure 15, we show the dust extinction calculated by SINOPSIS for the stars older than 2×10^7 yr. The highest values are reached in the same position where the extinction from the emission lines is also maximum. The ratio between the two extinction values is in general <2, as found e.g., in Calzetti et al. (2000; but see also Wuyts et al. 2013 for slightly lower values), but it reaches higher values in a small fraction of pixels, probably due to the galaxy geometry.

These maps only give a proxy for the presence of dust, as they do not take into account the 3D structure of the galaxy, projection effects, and the fact that the most dusty regions can be completely invisible at optical wavelengths.

Deriving the amount of dust from attenuation maps in the optical is doable but prone to the aforementioned uncertainties and is best done by means of radiative transfer models (see e.g., Popescu & Tuffs 2002; Baes et al. 2010; De Geyter et al. 2014; Saftly et al. 2015, and references therein), which are well beyond the goals of this work.

A much more reliable way, as opposed to the extinction map, is to look at the dust thermal emission showing up at far-infrared and submillimeter wavelengths.

JO36 is located within a field recently observed with the infrared space observatory *Herschel* (Pilbratt et al. 2010) as

Table 6
Flux Densities and Corresponding Uncertainties, in Jansky, Measured on the Five *Herschel* Bands from Archival Images

λ (μm)	Flux	Error
100	0.77	0.05
160	1.01	0.08
250	0.47	0.04
350	0.20	0.02
500	0.07	0.01

part of the program KPOT_mjuvela_1 (P.I. Mika Juvela, Juvela 2007). These observations, taken with both the PACS (Poglitsch et al. 2010) and SPIRE (Griffin et al. 2010) instruments, reveal an intense infrared emission detected at all wavelengths (100, 160, 250, 350, and 500 μm).

We reduced both PACS and SPIRE data in two steps, with the first one making use of the latest version of hipe (v14.2.0) to get the data to Level1, while the map making, de-glitching, and baseline removal were performed with the latest version of the IDL package SCANAMORPHOS (v25; Roussel 2013). We measured fluxes in apertures encompassing the whole galaxy in all maps, performing background subtraction as customary for such kinds of data (see, e.g., Ciesla et al. 2012; Verstappen et al. 2013; Cortese et al. 2014).

The much lower spatial resolution of *Herschel* data (the highest resolution is reached for PACS at 100 μm and is about 6″), when compared to optical images, makes it very hard to establish a spatial connection between the geometrical distribution of the dust and that of the ionized gas, as derived from MUSE data. Nevertheless, we can calculate a global estimate of the total dust mass and use this value to infer the gas mass.

Dust mass can be derived by means of SED fitting using a modified blackbody model emission. In Table 6 we report the measured infrared fluxes used for the modeling.

Figure 16 shows the infrared (IR) data points and the fit by means of a standard modified blackbody model, whose parameters are the mass of dust (i.e., the normalization), the dust temperature, and the dust emissivity. The latter is parametrized through the emissivity index, β, as defined in the following:

$$F_\nu = M_D k_{\nu_0} \left(\frac{\nu}{\nu_0}\right)^\beta \frac{B_\nu(T)}{D^2}, \quad (3)$$

where M_D is the dust mass, k_{ν_0} is the dust emissivity coefficient at a reference frequency ν_0, D is the distance to the galaxy, and B_ν is the Planck function (see, e.g., Smith et al. 2010a for an application of this method to local galaxies). Although simplistic, this fitting approach has been widely used in the literature and has been proven to give a fair physical approximation of the dust emission characteristics (Bianchi 2013).

As for the dust emissivity coefficient, we adopted the standard one from Draine (2003), which has a value of 0.192 $m^2\,kg^{-1}$ at 350 μm. The dust mass derived in this way ranges from $\sim 6 \times 10^7$ to $\sim 10^8\ M_\odot$. More specifically, if we leave the emissivity index β as a free parameter, we find a best fit for a dust temperature of 21.42 ± 1.80 K, an emissivity index $\beta = 2.17 \pm 0.32$, and a dust mass of $9.8^{+2.2}_{-1.8} \times 10^7\ M_\odot$. Integrating the blackbody model SED over the 10–1000 μm range, we get an IR luminosity of $2.59 \times 10^{10}\ L_\odot$. We convert this into an SFR using the Kennicutt (1998) relation, rescaled to the Chabrier (2003) IMF using the conversion factor as in Hayward et al. (2014):

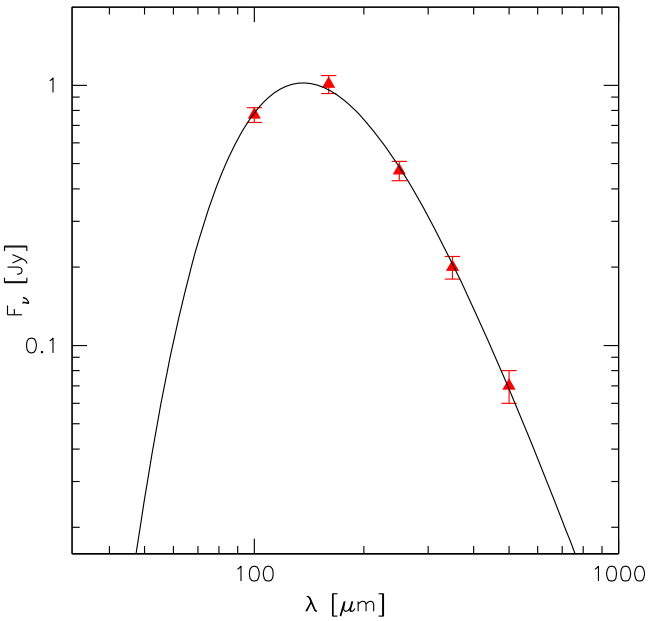

Figure 16. Modified blackbody fit (black line) to the observed *Herschel* data points (red triangles). A dust temperature of 20.63 K, $\beta = 2.15$, and dust mass of $9.8 \times 10^7\ M_\odot$ are derived from this model.

$$\mathrm{SFR_{IR}} = 3.0 \times 10^{-37} L_{\mathrm{IR}}\ \ M_\odot\ \mathrm{yr}^{-1}, \quad (4)$$

where L_{IR} is expressed in W (note that the aforementioned conversion factor is actually calculated for a Kroupa 2001 IMF, which anyway has a minimal difference with respect to the IMF we adopt here; see, e.g., Madau & Dickinson 2014). The SFR calculated in this way is 2.98 $M_\odot\ \mathrm{yr}^{-1}$.

Using a lower value for β (1.5), the dust mass we obtain is slightly lower, $5.8 \times 10^7\ M_\odot$ (and has a higher temperature compared to the previously found value, namely $T = 26.72$ K), but the 160 μm point is underestimated by more than 20%, well beyond the flux uncertainty in this band.

Following Eales et al. (2012) and using their Equation (2), we can derive the total gas mass (i.e., the mass of the gas in all phases) from submillimeter fluxes. Using the 500 μm flux and assuming the Galactic gas-to-dust ratio, we get a value of $3.2 \times 10^9\ M_\odot$. Similarly, following a much direct and straightforward approach, we can simply convert the dust mass into a gas mass of about $10^{10}\ M_\odot$ assuming the same Galactic gas-to-dust ratio of 100. Both values of the gas mass are quite consistent with those expected, within the observed dispersion, in normal, non-starbursting galaxies of similar stellar mass to JO36 (see, e.g., Magdis et al. 2012; Morokuma-Matsui & Baba 2015) and might give an indication that the majority of the gas is still retained by the galaxy.

This, of course, heavily relies on the assumption of a given gas-to-dust ratio that, for a galaxy in a cluster environment, might not be strictly true. Cortese et al. (2010), studying the spatially resolved dust emission versus the gas content on a sample of galaxies in the Virgo cluster, found evidence of dust-truncated disks in highly H I-deficient galaxies ($\mathrm{def_{H\,I}} > 0.87$). The fact that we observe such a high value of the dust mass can be hence taken as an indication that the amount of atomic gas

that has been stripped must yield a deficiency value smaller than 0.87. Using the definition of H I deficiency given by Chung et al. (2009) and assuming the aforementioned value for $\mathrm{def_{H\,I}}$, we can calculate a lower limit for the H I mass in JO36. The value we derive in this way is $\sim 1.4 \times 10^9\ M_\odot$. Again, this value compares very well to the H I mass expected for galaxies with similar stellar masses (see, e.g., Popping et al. 2014; Jaskot et al. 2015).

Using PACS data at 100 μm, which are those with the highest spatial resolution at these wavelengths, welooked for evidence of a possible truncation in the dust disk. Convolving the Hα image to the same 6″ resolution and regridding the map obtained in this way to the same pixel size, we found a somewhat good match between its extension and the one observed from 100 μm emission. Despite this, we cannot claim that there is a truncated dust disk, as *Herschel* images for this data set are made with only one cross-scan and the data are quite shallow. For this reason, it is more difficult to detect IR emission in the galaxy's outskirts, where dust is not only less abundant (in part due to weaker projection effects as well), but also colder.

If, instead, we look at the total extinction map (i.e., the extinction value calculated over all of the stellar ages, whose detection does not rely on the presence of emission lines) as derived by SINOPSIS, we note that dust seems to be present throughout the entire disk, affecting the starlight to different degrees depending on the position.

To determine the mass of the ionized gas, we used the relation between Hα luminosity and the mass of ionized hydrogen, as described in Poggianti et al. (2017). This also depends on the electron density, which we calculated from the ratio of the sulfur forbidden doublet at 6714 and 6731 Å. To calculate it, we adopted the prescription given in Proxauf et al. (2014),

$$n_e = 0.0543 \cdot \tan(-3.0553 \times R + 2.8506) + 6.98 - 10.6905 \times R + 9.9186 \times R^2 - 3.5442 \times R^3, \quad (5)$$

where $R = F_{6714}/F_{6731}$ is the ratio between the fluxes of the two lines (Poggianti et al. 2017). Equation (5) is valid in the range $0.436 \leqslant R \leqslant 1.435$. We used the line fluxes measured by KUBEVIZ and, when R assumes a value outside the two limits, we adopted a value equal to the closer limit. In case neither of the two lines was measurable, we took $R = 0.966$, which is the average between the upper and lower limits. As for the Hα flux, we used the value measured by KUBEVIZ on the absorption-corrected spectra. The effect of dust attenuation was also corrected for by using the value A_V that SINOPSIS provides for the young (i.e., line-emitting) stellar populations. This has the advantage that an extinction value is given also when Hβ is not available because it is too faint. No extinction correction was applied in case A_V was not calculated for a given spaxel. The total ionized gas mass computed in this way amounts to $6.9 \times 10^8\ M_\odot$. This mass is 2σ lower than the average value expected for galaxies of similar stellar mass (Popping et al. 2014).

JO36 is also detected by the NVSS radio survey (Condon et al. 1998) and has a (broad-band) flux density of 4.3 ± 0.5 mJy at 1.4 GHz. The emission in this band is dominated by the radio continuum, and it is therefore another tracer of the ionized gas. In Figure 17, we present IR data together with the radio (1.4 GHz) contours superimposed. The long radio tail is likely related to the nearby BCG (VV 382 or GIN 049), and there is a clear detection at the position of JO36.

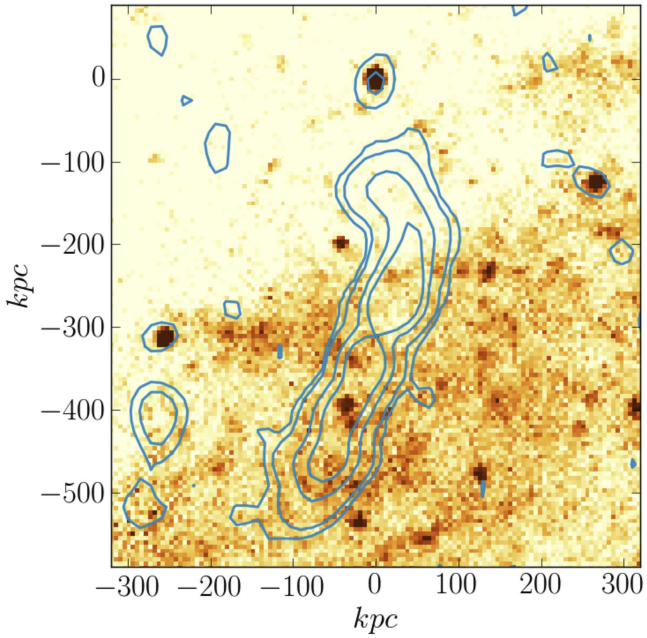

Figure 17. SPIRE 250 μm emission and radio contours (continuum emission at 1.4 GHz from Condon et al. 1998) of the region of the sky surrounding JO36.

These data can be used to derive another, independent estimate of the ionized gas mass. Using the prescription given in Galván-Madrid et al. (2008), which assumes that the gas is homogeneously distributed within a sphere, we find a value that is two orders of magnitude higher with respect to the previously calculated one, meaning that the assumptions made regarding the geometrical distribution of gas are probably too strong, and this method cannot be applied to a jellyfish like JO36 to derive the ionized gas mass. Emission from supernovae at these frequencies might also bias the result.

A further estimate of the SFR can be given using this data, with the advantage that this tracer is insensitive to dust extinction. With a luminosity $L_{1.4} = 1.67 \times 10^{22}\ \mathrm{W\,Hz^{-1}}$ and using the prescription from Hopkins et al. (2003; see their Equations (1) and (2)), we find an SFR of $9.2\ M_\odot\ \mathrm{yr^{-1}}$.

To summarize, we derived total gas masses from IR and submillimeter data in the range between 3.2×10^9 and $10^{10}\ M_\odot$. Both estimates rely on the assumption that a Galactic gas-to-dust ratio can be used for this galaxy. A lower limit of $1.4 \times 10^9\ M_\odot$ to the H I mass was extrapolated from the substantial presence of dust that we used as an indicator of the maximum degree of H I deficiency. All of these values agree with the gas mass expectations in galaxies of similar stellar mass. The exception to this is the ionized gas mass, which is lower by more than 2σ when compared to the average relation for similar galaxies.

The SFR calculated from the spectral fitting is $\sim 5.9\ M_\odot\ \mathrm{yr^{-1}}$ and naturally takes into account and hence corrects for the effect of dust attenuation. This SFR value depends on the intensity of the Hα line and, even when corrected for attenuation, might miss a completely embedded star formation component (e.g., Leroy et al. 2008). Saftly et al. (2015), for example, demonstrated that small-scale inhomogeneities and structures in the ISM distribution (which could host severely obscured star formation) can have a negligible effect on the

optical extinction, but their presence is revealed from their mid- and far-IR emission.

On the other hand, converting the IR emission into an SFR yielded $\sim 3\ M_{\odot}\ \mathrm{yr}^{-1}$. Deriving a value of the integrated SFR that includes both components (i.e., extinction-corrected plus completely obscured) is not straightforward: the timescales of star formation that they sample are quite different, with Hα being a tracer sensitive to the "instantaneous" star formation (i.e., stars younger than $\sim 10^7$ yr) and the IR tracing star-forming activity within 10^8 yr.

To be able to properly take these two components into account, we calculated the UV flux expected from the SINOPSIS model (no *GALEX* data are available for this galaxy) and exploited it to derive the unobscured SFR component. Using the prescription given in Kennicutt & Evans (2012), we calculate a non-obscured SFR value of $3.4\ M_{\odot}\ \mathrm{yr}^{-1}$, which, as UV bands typically sample timescales very close to those of the IR, we can add to the value calculated from the dust emission. Doing so, we get an SFR of $6.4\ M_{\odot}\ \mathrm{yr}^{-1}$, over a 100 Myr timescale.

An extinction-independent value for the SFR is given by the radio continuum, from which we calculated a value of $9.2\ M_{\odot}\ \mathrm{yr}^{-1}$, which significantly higher with respect to the aforementioned estimates. The discrepancy with respect to the previously calculated values might come from the presence of an AGN (see Section 5.4), even though one of relatively low luminosity, which could indeed boost the radio emission.

7. Discussion

The most important results we have obtained so far can be summarized as follows.

1. The stellar disk extends out to a radius of about 25 kpc, while the ionized gas only reaches galactrocentric distances of about 15 kpc. We interpret this as clear evidence of a truncated ionized gas disk.
2. A stellar tail, extending $\sim$5 kpc with respect to the main body of the disk, is observed toward the south.
3. Four Hα blobs are present southwards of the galaxy, close to the aforementioned tail.
4. The (ionized) gas velocity field is noticeably distorted, especially when compared to the stellar one.
5. The dust mass is compatible with that expected in "normal" field galaxies having similar stellar masses. This strongly suggests that dust has not been stripped. If dust is used as a tracer for the presence of gas, we infer a total gas mass in the range expected for the physical characteristics of this galaxy. The fact that no evidence of significant dust stripping is found constrains the H I deficiency level of the galaxy, and this was used to estimate a lower limit of the H I mass.
6. The mass of ionized gas is at the lower limit with respect to the value expected for galaxies of similar stellar mass.
7. Star formation is currently happening only in the central region of the galaxy, within a 10 kpc radius, while the external ($r > 10$ kpc) parts of the disk are dominated by stars with ages $<$500 Myr.
8. The star formation history of the galaxy shows evidences of an inside-out formation process. An enhancement in the SFR happened between 20 and 500 Myr ago, more deeply affecting the outer disk than the central regions.

In the next section, Section 7.1, we present various pieces of evidence of active ram pressure in this galaxy, while in the following sections we try to build a self-consistent picture that can interpret the aforementioned observed features simultaneously.

7.1. Strength of the Ram Pressure in JO36

Given JO36's vicinity to the core of A160 and its high velocity within the cluster (see the phase–space diagram, as in Jaffé et al. 2015, shown in Figure 18), it is likely that ram pressure stripping (RPS) is or has been at play. The ram pressure by the ICM can be estimated as $P_{\mathrm{ram}} = \rho_{\mathrm{ICM}} \times v_{\mathrm{cl}}^2$ (Gunn & Gott 1972), where $\rho_{\mathrm{ICM}}(r_{\mathrm{cl}})$ is the radial density profile of the ICM, r_{cl} the clustercentric distance, and v_{cl} the velocity of the galaxy with respect to the cluster. Since A160 is a low-mass cluster (velocity dispersion $= 561\ \mathrm{km\ s}^{-1}$), we assume a smooth static ICM similar to that of the Virgo cluster. Utilizing the density model used by Vollmer et al. (2001), we can get an estimate of the ram pressure at the projected r_{cl} and line-of-sight velocity of JO36,

$$P_{\mathrm{ram}} = 9.5 \times 10^{-14}\ \mathrm{Nm}^{-2}. \quad (6)$$

To assess whether this is enough to strip gas from JO36, we compute the anchoring force of the galaxy assuming an exponential disk density profile for the stars and the gas components (Σ_s and Σ_g respectively) defined as

$$\Sigma = \left(\frac{M_d}{2\pi r_d^2}\right) e^{-r/r_d}, \quad (7)$$

where M_d is the disk mass, r_d the disk scale-length, and r the radial distance from the center of the galaxy. For the stellar component of JO36, we adopted a disk mass $M_{d,\mathrm{stars}} = 5.2 \times 10^{10}\ M_{\odot}$ (accounting for a bulge to total ratio of 0.2) and a disk scale-length $r_{d,\mathrm{stars}} = 4.63$ kpc, obtained by fitting the light profile of the galaxy. For the gas component, we assumed a total mass $M_{d,\mathrm{gas}} = 0.1 \times M_{d,\mathrm{stars}}$, and scale-length $r_{d,\mathrm{gas}} = 1.7 \times r_{d,\mathrm{stars}}$ (Boselli & Gavazzi 2006).

The anchoring force in the disk can then be computed as $\Pi_{\mathrm{gal}} = 2\pi G \Sigma_g \Sigma_s$ at different radial distances from the center of the galaxy (r). We find that the condition for stripping is met at $r \sim 13.4$ kpc, where Π_{gal} drops below P_{ram}. This truncation radius corresponds to $\sim$21% of the total gas mass stripped (see the reference dashed line in the right panel of Figure 18).

The estimated fraction of stripped gas is consistent with the lower limit of H I mass derived in Section 5 (from the dust content), which, when compared to the gas mass in our disk model, yields an upper limit for the fraction of stripped gas of $\sim$27%. It is also interesting to compare the expected stripping from our modeling with the observed truncation radius. Taking the extent of Hα emission as a good estimate, we get an observed truncation radius of $r_t = 11$ kpc, which corresponds to more stripping than predicted ($\sim$27% of the total gas mass; solid blue line in Figure 18). We note, however, that the predicted stripping suffers from uncertainties in the galaxy and cluster model, and projection effects, and that it does not take into account possible inhomogeneities of the ICM.

To test for the presence of substructures within the cluster, we selected galaxies with significant deviations from the cluster velocity dispersion (colored symbols) and found that JO36 does not belong to any clear group. A dynamical analysis of A160 (Biviano et al. 2017) reveals several substructures, shown

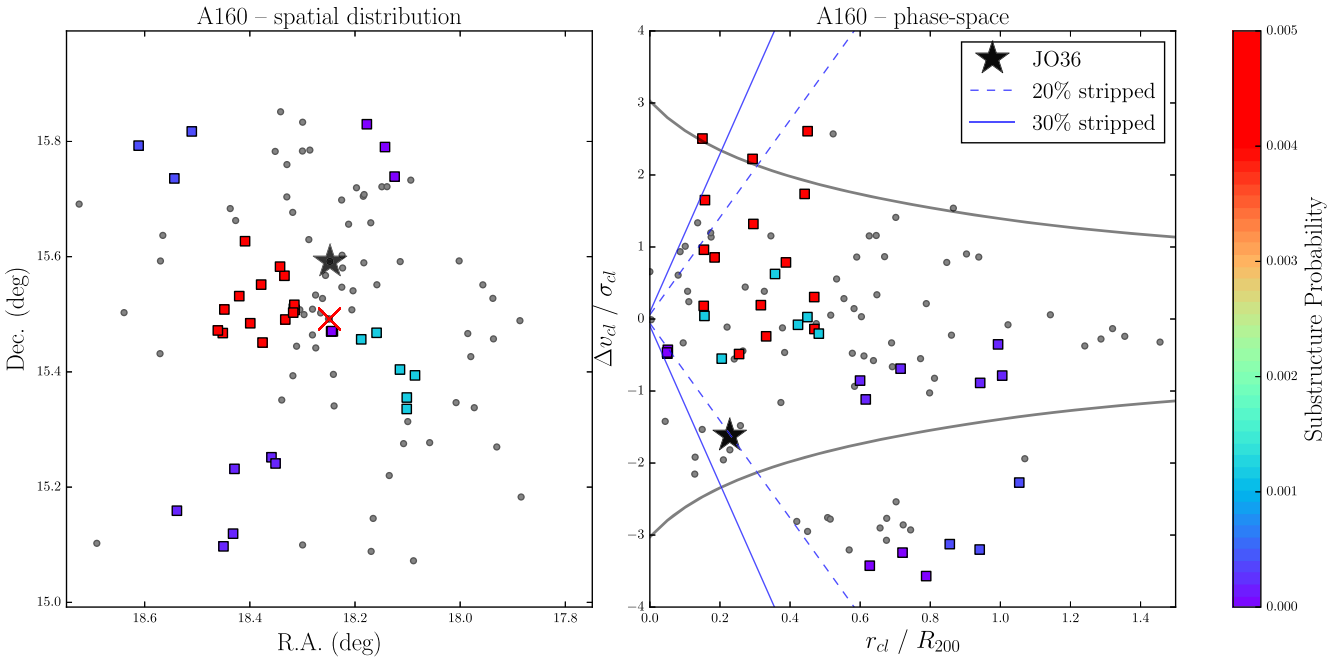

Figure 18. Left: position in the sky of the JO36 spectroscopic members from OmegaWINGS (small gray points), JO36 (star), and the BCG (red cross). Squares correspond to identified substructures, which have been color-coded according to their probability of being random fluctuations (i.e., values close to zero indicate highly significant substructure detections; Biviano et al. 2017). Right: phase–space diagram with symbols as in the left panel. Curves show the escape velocity in a Navarro et al. (1997) halo. The dashed and solid blue lines correspond to 20% and 30% of the total gas mass stripped in JO36 by the ICM in a Virgo-like cluster (see the text for details).

with colored squares in Figure 18. However, there is no evidence for JO36 residing in any of these substructures. On the contrary, its phase–space position suggests that this galaxy has recently fallen into the cluster as an isolated galaxy.

Overall, our analysis shows that JO36 must have lost between ∼20% and 30% of its total gas mass via ram pressure stripping by A160's ICM.

We now propose two mutually exclusive scenarios, each of which is successful in explaining some of the observed features listed above while, at the same time, failing to account for others. The difference in the two scenarios simply lies in the direction of the tangential velocity of the galaxy.

7.2. Tangential Velocity Toward the North (1)

JO36 was selected as a possible jellyfish candidate because of the presence of a tail, pointing toward the location of the BCG, visible in WINGS *V*- and *B*-band images. This, together with the detection of a few relatively bright Hα spots located close to this tail, are features that we recover in MUSE data as well (see the left panel of Figure 5 for the tail and the right panel in the same figure for the blobs).

These features can be explained in a scenario where the galaxy has a velocity component in the direction opposite to the location of both the tail and the blobs, moving away from the cluster center (the direction toward the X-ray center and the location of the BCG are indicated by the two arrows in Figure 5). In this picture, the denser gas in the central regions of the cluster exerted an RPS force capable of ripping part of the gas away from the galaxy, which would be now found in the form of the observed Hα-emitting blobs. Something very similar, although to a much more spectacular degree, is observed in other jellyfish galaxies (e.g., Merluzzi et al. 2013, 2016; Fumagalli et al. 2014; Bellhouse et al. 2017; Poggianti et al. 2017), where bright tails and star-forming blobs are found in locations opposite the direction of the galaxy motion. Just like the aforementioned cases, the blobs we observe here retain the disk velocity.

7.3. Tangential Velocity Toward the South (2)

Although scenario (1) is the most likely explanation for the star-forming blobs, there are a number of other observed features that it cannot account for.

Analyzing Figure 5, we already pointed out how the locus where the gas has a zero radial velocity component is twisted into an irregular "U" shape, with a concavity directed toward the north, and it reaches galactocentric radii of about 8 kpc toward the same direction. Similarly, gas with positive radial velocities is found on the same side (the region labelled "F" in Figure 5). This twisting of the gas rotational axis is a feature that is predicted as a consequence of RPS by the aforementioned simulations of Merluzzi et al. (2016), where the direction of the bending is directly related to the velocity of the galaxy on the plane of the sky. This, in the case of JO36, would be pointing to the cluster center.

This scenario would also explain why the star-forming region, clearly visible in the right panel of Figure 8, is slightly bent in a "C" shape pointing toward the southeast and offset, with respect to the stellar continuum, in that direction. If shocks between the gas within the galaxy and the gas in the intracluster gas are responsible for the enhanced star formation, it is hence logical to expect that this would happen first in the direction of the interaction between the two gas components, which, in this scenario, would be on this side of the disk.

7.4. More than Just One Mechanism at Play?

JO36 shows a clear signature of past and ongoing RPS. This is further confirmed by the phase–space diagram (Figure 18)

that shows that the galaxy is well within the region where ram pressure is strong enough to eventually strip all of the gas.

Hence, although it is quite clear that we are observing RPS signatures, scenario (2) cannot naturally explain the presence of the four gas blobs for which we would need to appeal to other phenomena. On the other hand, scenario (1) seems to be partially in contradiction with the gas velocity map. Such a distortion naturally arises due to RPS if the galaxy were moving in the opposite direction, i.e., toward the cluster center.

Furthermore, the stellar tail, visible in Figure 5, does not fit either of the two proposed scenarios and needs other physical mechanisms to be invoked. Although a morphological feature clearly departing from the disk, it does not seem to have any counterpart with similar characteristics in the north side of the galaxy. Moreover, the (stellar) velocities follow the trend observed in the disk itself, as expected if this were a natural continuation of the disk, and have the highest values found in the galaxy.

If this tail were the result of gas stripping from the outer disk by ram pressure, one would expect that it retains a similar velocity with respect to the region within the disk where it came from. The measured velocities are higher by up to $50\,\mathrm{km\,s^{-1}}$ with respect to the rest of the disk (see also the rotation curve in Figure 6).

In addition, the average age of the stellar populations of this tail is compatible with a formation epoch up to 500 Myr ago, and hence significantly older with respect to the ages derived for the blobs that are rich in ionized gas and still actively star forming. If this were to happen in a stripped gas component, we would not be observing it still attached to the galaxy, as the gas would have had the time to move away and detach from the galaxy's disk. On the other side, stars are not affected by RPS.

For these reasons, we can conclude that RPS cannot be the mechanism by which this stellar tail originated, and we would need to invoke a different mechanism to explain its formation.

According to numerical simulations performed by Kronberger et al. (2008a) that aimed to study the effect of ram pressure on the star formation of spiral galaxies, the observed enhanced star formation rate in stellar populations with ages in the 20–500 Myr range is a direct effect of the interaction between the gas in the galaxy and that in the ICM. This would somehow date the beginning of the interaction between the galaxy and the hot gas in the cluster.

Following the same authors, when the interaction is "edge on," such as in our case, the gas loss is much lower compared to a face-on interaction, the main signature of ram pressure being a distortion and compression in the gas disk, which is indeed what we observe. Enhanced SFRs by up to a factor of 3 are observed in these simulations, compatible with the values we derived by spectral fitting (see also Koopmann & Kenney 2004).

Numerical simulations from the same group (Kronberger et al. 2008b), focusing on the effects on the rotation curves and velocity fields of the gas, show a stronger distortion of the gas distribution in edge-on interactions compared to the face-on case. They also observe a displacement on the rotation axis of stars and gas, something that we do not find.

Integrating the observed datacube with respect to the wavelength coordinate, we get a high S/N picture that better allows the morphology of the lowest surface brightness components of the galaxy (Figure 9) to be viewed. By doing this, we can confirm the absence of a tidal feature in the northern disk, while two of the Hα blobs appear to be almost embedded within the disk, making it unclear whether they effectively are jellyfish morphological features or nothing more but regions of residual star formation from a quenched disk. Nevertheless, the brightest and largest blobs (A and D) are, even in projection, too far away to fill in this picture.

Different methods to infer the gas mass yielded values in fairly good agreement with respect to each other, and these point to a regular gas-to-stellar mass content.

In any case, given the relatively low mass of the A160 cluster ($L_X = 10^{43.6}\,\mathrm{erg\,s^{-1}}$, Ebeling et al. 1996, and $\sigma_{\mathrm{gal}} = 561\,\mathrm{km\,s^{-1}}$, Moretti et al. 2017), and given the dependency of the RPS effect on the cluster gas density, we do not expect, at least as long as short timescales are concerned, massive gas losses, most of all given the geometry of the galaxy motion (numerical simulations by Kronberger et al. 2008a have shown that edge-on systems are much less prone to gas loss) and the mass of the galaxy.

One possible explanation for the extended stellar disk (i.e., the tail) is that it could be the result of a localized interaction. Kronberger et al. (2006) performed numerical simulations to study how galaxy encounters influence the kinematics of stellar disks. For given sets of simulations parameters, they find that a fly-by can affect the stellar rotation in the disk outskirts in different ways depending on the configuration of the encounter and on the line of sight of the observation. Some of the rotation curves they extract from their simulations resemble the asymmetry we observe in JO36 stellar kinematics and, in particular, in the tail. Similarly, Pedrosa et al. (2008) claim that bifurcations, i.e., asymmetries in the outer parts of a rotation curve, such as those we observe in JO36, are a clear indicator of a recent galaxy encounter.

It would be tempting to identify in one of the blobs (e.g., blob A, the most massive one) the possible candidate for this kind of interaction. In this case, we would be witnessing the later phases of an encounter between JO36 and a dwarf galaxy. Nevertheless, the metallicity[12] values we derive for blob A are way too high to be compatible with those of a dwarf system, being instead fully consistent, within the typical uncertainties, with the metallicity of the outer gas that remains for now in the disk.

8. Summary and Conclusions

In this work, we undertook an analysis of the properties of the stellar populations and of the interstellar medium in JO36, a galaxy in the Abel 160 cluster, with slightly distorted optical morphology, which is possibly a signature of gas stripping. We used these observations to validate our spectral fitting code, SINOPSIS, for applications to IFU data analysis by comparing its results with those obtained from GANDALF, a well-known and widely used code generally exploited to derive the properties of emission lines and of the underlying stellar populations. This comparison indicates that our approach gives robust results fully compatible with those obtained with GANDALF on the same data set.

From the results of the kinematic analysis and of the stellar population properties in this galaxy, we draw the following conclusions.

[12] Metallicities are calculated throughout the whole galaxy by means of the *pyqz* code by Dopita et al. (2013). Further details on this issue can be found in Poggianti et al. (2017), but see also Kewley & Ellison (2008) 4for absolute uncertainties assessment.

1. JO36 shows no spectacular morphological signatures of gas stripping such as those commonly encountered in the so-called jellyfish galaxies, but the ionized gas disk is clearly truncated with respect to the stellar one.
2. If any gas stripping has occurred in the past, it most likely involved a minor fraction of the total gas in the galaxy. Substantial gas depletion due to an intense star-forming episode that happened about 500 Myr ago could have contributed to the creation of the truncated ionized gas disk.
3. From a kinematical point of view, the rotation curve of the gas displays asymmetries in the outer parts of the disk, with a rotation axis strongly distorted and suggestive of a velocity component toward the center of the cluster. This is in agreement with numerical simulations of RPS acting with a relative velocity parallel to the galaxy plane (edge-on).
4. The presence of Hα blobs close to the southern edge of the galaxy might suggest a tangential velocity component in the north direction, something that seems to be incompatible with the morphological characteristics of the gas rotational axis.
5. The presence of a stellar tail in the southern disk, with no clear counterpart in the opposite direction, cannot be attributed to ram pressure effects. Its velocities follow the stellar rotation curve from the inner parts and are higher than those measured across the entire galaxy disk. Composed of stellar populations of ages between 2×10^7 and 5×10^8 yr and showing no evidence for the presence of gas, it can be the result of a gravitational interaction with a less massive galaxy, as suggested by numerical simulations.
6. There is no evidence of AGN activity, at least as far as diagnostic lines are concerned. However, the detection of a strong emission in the X-rays strongly suggests the possible presence of a deeply obscured AGN (F. Nicastro et al. 2017, in preparation).

JO36 is a moderately massive spiral that is subject to RPS as several pieces of evidence suggest. The truncated ionized gas disk, the low ratio of H II/M_* with respect to similar galaxies, the disturbed gas kinematics, the presence of ionized gas regions clearly detached from disk, its location on the phase–space diagram of the cluster, and finally an episode of enhanced star formation strongly involving the outer disk all point to ram pressure being caught in the act.

We also speculate that the stripped gas is probably a minor fraction of the gas in the galaxy. By indirect calculations of the amount of total gas and of H I, we find that the gas content is quite typical, given the stellar mass of the galaxy. Furthermore, the moderately intense star formation likely induced by shocks between the gas within the galaxy and the one in the ICM, has consumed a substantial amount of gas. Indeed, in the analysis of their numerical simulations, Kronberger et al. (2008a) propose that loss of gas by RPS, together with depletion due to star formation, is the reason for the decrease, and eventual quenching, of the star formation rate.

What is less clear is instead the direction of the ram pressure or, equivalently, of the galaxy motion within the cluster. In fact, we could not reconcile in a self-consistent manner the presence of ionized gas in the southern part of the galaxy, which indicates a velocity component toward the north, with the distorted shape of the gas rotational axis, which suggests instead a velocity component toward the south. Dedicated numerical simulations are probably the best tool to figure out the kinematics of the galaxy and give hints on its orbit to better understand the relation between its star formation history and the interaction with the cluster environment.

With respect to the first point in our final remarks, it should be noted that the MUSE data for this galaxy basically cover all of its disk but we cannot draw any conclusion on the possible presence of stripped tails at larger distances, which passed unobserved in optical images. Furthermore, we lack H I data to derive the atomic mass distribution and to give a final word on the dynamical history of the galaxy.

Both Poggianti et al. (2016) and McPartland et al. (2016) stress the importance of spectroscopic data to unveil the occurrence of gas-stripping signatures as opposed to pure photometric detections. In this particular case, the MUSE data turned out to be critical to uncover a second dynamical mechanism affecting this galaxy, most likely a gravitational interaction with a much less massive galaxy.

We would like to thank the anonymous referee, whose suggestions and criticism helped us improve the quality and presentation of the results of the paper. Based on observations collected at the European Organisation for Astronomical Research in the Southern Hemisphere under ESO programme 196.B-0578. J.F. warmly thanks Anna Feltre for all of the advice in running CLOUDY, Theodoros Bitsakis for stimulating discussions, and Raul Naranjo and Daniel Díaz Gonzalez who helped with some of the technicalities in SINOPSIS.

J.F. acknowledges financial support from the UNAM-DGAPA-PAPIIT IA104015 grant, México. G.B. acknowledges support for this work from UNAM through grant PAPIIT IG100115. This work was co-funded under the Marie Curie Actions of the European Commission (FP7-COFUND) B.V. acknowledges support from an Australian Research Council Discovery Early Career Researcher Award (PD0028506). B.C.S. acknowledges financial support through PAPIIT project IA103517 from DGAPA-UNAM.

Software: SINOPSIS, gandalf (Sarzi et al. 2006), cloudy (Ferland 1993; Ferland et al. 1998, 2013), kubeviz (Fossati et al. 2016), pPXF (Cappellari & Emsellem 2004; Cappellari 2012), pyqz (Dopita et al. 2013), scanamorphos (Roussel 2013), HIPE, IDL, Python.

ORCID iDs

Jacopo Fritz https://orcid.org/0000-0002-7042-1965
Alessia Moretti https://orcid.org/0000-0002-1688-482X
Marco Gullieuszik https://orcid.org/0000-0002-7296-9780
Bianca Poggianti https://orcid.org/0000-0001-8751-8360
Gustavo Bruzual https://orcid.org/0000-0002-6971-5755
Benedetta Vulcani https://orcid.org/0000-0003-0980-1499
Fabrizio Nicastro https://orcid.org/0000-0002-6896-1364
Bernardo Cervantes Sodi https://orcid.org/0000-0002-2897-9121
Daniela Bettoni https://orcid.org/0000-0002-4158-6496
Andrea Biviano https://orcid.org/0000-0002-0857-0732
Stéphane Charlot https://orcid.org/0000-0003-3458-2275
Callum Bellhouse https://orcid.org/0000-0002-6179-8007

References

Abramson, A., Kenney, J., Crowl, H., & Tal, T. 2016, AJ, 152, 32
Athanassoula, E. 2002, ApJL, 569, L83
Bacon, R., Copin, Y., Monnet, G., et al. 2001, MNRAS, 326, 23
Baes, M., Verstappen, J., De Looze, I., et al. 2010, A&A, 518, L39
Balogh, M. L., Navarro, J. F., & Morris, S. L. 2000, ApJ, 540, 113
Bellhouse, C., Jaffé, Y. L., Hau, G. K. T., et al. 2017, ApJ, 844, 49
Berta, S., Fritz, J., Franceschini, A., Bressan, A., & Pernechele, C. 2003, A&A, 403, 119
Bianchi, S. 2013, A&A, 552, A89
Bischko, J. C., Steinhauser, D., & Schindler, S. 2015, A&A, 576, A76
Biviano, A., Moretti, A., Paccagnella, A., et al. 2017, arXiv:1708.07349
Boselli, A., & Gavazzi, G. 2006, PASP, 118, 517
Boselli, A., Roehlly, Y., Fossati, M., et al. 2016, A&A, 596, A11
Bressan, A., Marigo, P., Girardi, L., et al. 2012, MNRAS, 427, 127
Burrows, A. 2000, Natur, 403, 727
Byler, N., Dalcanton, J. J., Conroy, C., & Johnson, B. D. 2017, ApJ, 840, 44
Byrd, G., & Valtonen, M. 1990, ApJ, 350, 89
Calzetti, D., Armus, L., Bohlin, R. C., et al. 2000, ApJ, 533, 682
Calzetti, D., Kinney, A. L., & Storchi-Bergmann, T. 1994, ApJ, 429, 582
Cappellari, M. 2012, pPXF: Penalized Pixel-fitting Stellar Kinematics Extraction, Astrophysics Source Code Library, ascl:1210.002
Cappellari, M., & Copin, Y. 2012, Voronoi Binning Method, Astrophysics Source Code Library, ascl:1211.006
Cappellari, M., & Emsellem, E. 2004, PASP, 116, 138
Cardelli, J. A., Clayton, G. C., & Mathis, J. S. 1989, ApJ, 345, 245
Chabrier, G. 2003, PASP, 115, 763
Charlot, S., & Longhetti, M. 2001, MNRAS, 323, 887
Cheung, E., Bundy, K., Cappellari, M., et al. 2016, Natur, 533, 504
Chevallard, J., & Charlot, S. 2016, MNRAS, 462, 1415
Chung, A., van Gorkom, J. H., Kenney, J. D. P., Crowl, H., & Vollmer, B. 2009, AJ, 138, 1741
Cid Fernandes, R. 2007, IAUS, 241, 461
Cid Fernandes, R., Mateus, A., Sodré, L., Stasińska, G., & Gomes, J. M. 2005, MNRAS, 358, 363
Ciesla, L., Boselli, A., Smith, M. W. L., et al. 2012, A&A, 543, A161
Condon, J. J., Cotton, W. D., Greisen, E. W., et al. 1998, AJ, 115, 1693
Cortese, L., Davies, J. I., Pohlen, M., et al. 2010, A&A, 518, L49
Cortese, L., Fritz, J., Bianchi, S., et al. 2014, MNRAS, 440, 942
Cortese, L., Marcillac, D., Richard, J., et al. 2007, MNRAS, 376, 157
Cowie, L. L., & Songaila, A. 1977, Natur, 266, 501
Croton, D. J., Springel, V., White, S. D. M., et al. 2006, MNRAS, 365, 11
Crowl, H. H., & Kenney, J. D. P. 2008, AJ, 136, 1623
Debattista, V. P., & Sellwood, J. A. 2000, ApJ, 543, 704
De Geyter, G., Baes, M., Camps, P., et al. 2014, MNRAS, 441, 869
De Looze, I., Fritz, J., Baes, M., et al. 2014, A&A, 571, A69
de Zeeuw, P. T., Bureau, M., Emsellem, E., et al. 2002, MNRAS, 329, 513
Dopita, M. A., Sutherland, R. S., Nicholls, D. C., Kewley, L. J., & Vogt, F. P. A. 2013, ApJS, 208, 10
Draine, B. T. 2003, ARA&A, 41, 241
Dressler, A., Rigby, J., Oemler, A., Jr., et al. 2009, ApJ, 693, 140
Eales, S., Smith, M. W. L., Auld, R., et al. 2012, ApJ, 761, 168
Ebeling, H., Stephenson, L. N., & Edge, A. C. 2014, ApJL, 781, L40
Ebeling, H., Voges, W., Bohringer, H., et al. 1996, MNRAS, 281, 799
Fabian, A. C., Sanders, J. S., Allen, S. W., et al. 2003, MNRAS, 344, L43
Falcón-Barroso, J., Sánchez-Blázquez, P., Vazdekis, A., et al. 2011, A&A, 532, A95
Faltenbacher, A., & Diemand, J. 2006, MNRAS, 369, 1698
Fasano, G., Marmo, C., Varela, J., et al. 2006, A&A, 445, 805
Ferland, G. J. 1993, Hazy, A Brief Introduction to Cloudy 84, University of Kentucky Physics Department Internal Report
Ferland, G. J., Kisielius, R., Keenan, F. P., et al. 2013, ApJ, 767, 123
Ferland, G. J., Korista, K. T., Verner, D. A., et al. 1998, PASP, 110, 761
Fielding, D., Quataert, E., McCourt, M., & Thompson, T. A. 2017, MNRAS, 466, 3810
Fitzpatrick, E. L. 1986, AJ, 92, 1068
Fossati, M., Fumagalli, M., Boselli, A., et al. 2016, MNRAS, 455, 2028
France, K., McCray, R., Heng, K., et al. 2010, Sci, 329, 1624
Franzetti, P., Scodeggio, M., Garilli, B., Fumana, M., & Paioro, L. 2008, in ASP Conf. Ser. 394, Astronomical Data Analysis Software and Systems, ed. R. W. Argyle et al. (San Francisco, CA: ASP), 642
Fritz, J., Poggianti, B. M., Bettoni, D., et al. 2007, A&A, 470, 137
Fritz, J., Poggianti, B. M., Cava, A., et al. 2011, A&A, 526, A45
Fumagalli, M., Fossati, M., Hau, G. K. T., et al. 2014, MNRAS, 445, 4335
Galván-Madrid, R., Rodríguez, L. F., Ho, P. T. P., & Keto, E. 2008, ApJL, 674, L33
Griffin, M. J., Abergel, A., Abreu, A., et al. 2010, A&A, 518, L3
Guglielmo, V., Poggianti, B. M., Moretti, A., et al. 2015, MNRAS, 450, 2749
Gullieuszik, M., Poggianti, B., Fasano, G., et al. 2015, A&A, 581, A41
Gunn, J. E., & Gott, J. R., III 1972, ApJ, 176, 1
Gutkin, J., Charlot, S., & Bruzual, G. 2016, MNRAS, 462, 1757
Hayashi, M., Sobral, D., Best, P. N., Smail, I., & Kodama, T. 2013, MNRAS, 430, 1042
Hayward, C. C., Lanz, L., Ashby, M. L. N., et al. 2014, MNRAS, 445, 1598
Hohl, F. 1971, ApJ, 168, 343
Hopkins, A. M., Miller, C. J., Nichol, R. C., et al. 2003, ApJ, 599, 971
Jaffé, Y. L., Smith, R., Candlish, G. N., et al. 2015, MNRAS, 448, 1715
Jaskot, A. E., Oey, M. S., Salzer, J. J., et al. 2015, ApJ, 808, 66
Juvela, M. 2007, Herschel Space Observatory Proposal, 102
Kauffmann, G., Heckman, T. M., Tremonti, C., et al. 2003, MNRAS, 346, 1055
Kennicutt, R. C., & Evans, N. J. 2012, ARA&A, 50, 531
Kennicutt, R. C., Jr. 1998, ARA&A, 36, 189
Kewley, L. J., Dopita, M. A., Sutherland, R. S., Heisler, C. A., & Trevena, J. 2001, ApJ, 556, 121
Kewley, L. J., & Ellison, S. L. 2008, ApJ, 681, 1183
Kewley, L. J., Groves, B., Kauffmann, G., & Heckman, T. 2006, MNRAS, 372, 961
Koleva, M., Prugniel, P., Bouchard, A., & Wu, Y. 2009, A&A, 501, 1269
Koopmann, R. A., & Kenney, J. D. P. 2004, ApJ, 613, 866
Kronberger, T., Kapferer, W., Ferrari, C., Unterguggenberger, S., & Schindler, S. 2008a, A&A, 481, 337
Kronberger, T., Kapferer, W., Schindler, S., et al. 2006, A&A, 458, 69
Kronberger, T., Kapferer, W., Unterguggenberger, S., Schindler, S., & Ziegler, B. L. 2008b, A&A, 483, 783
Kroupa, P. 2001, MNRAS, 322, 231
Larson, R. B., Tinsley, B. M., & Caldwell, C. N. 1980, ApJ, 237, 692
Leroy, A. K., Walter, F., Brinks, E., et al. 2008, AJ, 136, 2782
Liu, G., Calzetti, D., Hong, S., et al. 2013, ApJL, 778, L41
MacArthur, L. A., González, J. J., & Courteau, S. 2009, MNRAS, 395, 28
Madau, P., & Dickinson, M. 2014, ARA&A, 52, 415
Magdis, G. E., Daddi, E., Béthermin, M., et al. 2012, ApJ, 760, 6
Marasco, A., Debattista, V. P., Fraternali, F., et al. 2015, MNRAS, 451, 4223
Marconi, A., Risaliti, G., Gilli, R., et al. 2004, MNRAS, 351, 169
Martinez-Valpuesta, I., Shlosman, I., & Heller, C. 2006, ApJ, 637, 214
McNamara, B. R., & Nulsen, P. E. J. 2007, ARA&A, 45, 117
McPartland, C., Ebeling, H., Roediger, E., & Blumenthal, K. 2016, MNRAS, 455, 2994
Merluzzi, P., Busarello, G., Dopita, M. A., et al. 2013, MNRAS, 429, 1747
Merluzzi, P., Busarello, G., Dopita, M. A., et al. 2016, MNRAS, 460, 3345
Mihos, J. C., & Hernquist, L. 1994, ApJL, 425, L13
Moore, B., Katz, N., Lake, G., Dressler, A., & Oemler, A. 1996, Natur, 379, 613
Moretti, A., Gullieuszik, M., Poggianti, B., et al. 2017, A&A, 599, A81
Morokuma-Matsui, K., & Baba, J. 2015, MNRAS, 454, 3792
Moustakas, J., Kennicutt, R. C., Jr., & Tremonti, C. A. 2006, ApJ, 642, 775
Navarro, J. F., Frenk, C. S., & White, S. D. M. 1997, ApJ, 490, 493
Ocvirk, P., Pichon, C., Lançon, A., & Thiébaut, E. 2006, MNRAS, 365, 46
Osterbrock, D. E., & Ferland, G. J. 2006, Astrophysics of Gaseous Nebulae and Active Galactic Nuclei (2nd ed.; Sausalito, CA: Univ. Science Books)
Paccagnella, A., Vulcani, B., Poggianti, B. M., et al. 2016, ApJL, 816, L25
Pacifici, C., Charlot, S., Blaizot, J., & Brinchmann, J. 2012, MNRAS, 421, 2002
Pedrosa, S., Tissera, P. B., Fuentes-Carrera, I., & Mendes de Oliveira, C. 2008, A&A, 484, 299
Piconcelli, E., Jimenez-Bailón, E., Guainazzi, M., et al. 2005, A&A, 432, 15
Pilbratt, G. L., Riedinger, J. R., Passvogel, T., et al. 2010, A&A, 518, L1
Poggianti, B. M., Bressan, A., & Franceschini, A. 2001, ApJ, 550, 195
Poggianti, B. M., Fasano, G., Omizzolo, A., et al. 2016, AJ, 151, 78
Poggianti, B. M., Moretti, A., Gullieuszik, M., et al. 2017, ApJ, 844, 48
Poglitsch, A., Waelkens, C., Bauer, O. H., et al. 2010, A&A, 518, L2
Popescu, C. C., & Tuffs, R. J. 2002, MNRAS, 335, L41
Popping, G., Somerville, R. S., & Trager, S. C. 2014, MNRAS, 442, 2398
Poznanski, D., Prochaska, J. X., & Bloom, J. S. 2012, MNRAS, 426, 1465
Proxauf, B., Öttl, S., & Kimeswenger, S. 2014, A&A, 561, A10
Ranalli, P., Comastri, A., & Setti, G. 2003, A&A, 399, 39
Risaliti, G., Maiolino, R., & Salvati, M. 1999, ApJ, 522, 157
Roussel, H. 2013, PASP, 125, 1126
Saftly, W., Baes, M., De Geyter, G., et al. 2015, A&A, 576, A31
Sánchez, S. F., Pérez, E., Sánchez-Blázquez, P., et al. 2016, RMxAA, 52, 21

Sánchez-Blázquez, P., Peletier, R. F., Jiménez-Vicente, J., et al. 2006, MNRAS, 371, 703
Sarzi, M., Falcón-Barroso, J., Davies, R. L., et al. 2006, MNRAS, 366, 1151
Sharp, R. G., & Bland-Hawthorn, J. 2010, ApJ, 711, 818
Silk, J., & Rees, M. J. 1998, A&A, 331, L1
Smith, M. W. L., Vlahakis, C., Baes, M., et al. 2010a, A&A, 518, L51
Smith, R. J., Lucey, J. R., Hammer, D., et al. 2010b, MNRAS, 408, 1417
Springel, V. 2000, MNRAS, 312, 859
Steinacker, J., Baes, M., & Gordon, K. D. 2013, ARA&A, 51, 63
Steinhauser, D., Haider, M., Kapferer, W., & Schindler, S. 2012, A&A, 544, A54
Steinhauser, D., Schindler, S., & Springel, V. 2016, A&A, 591, A51
Takeda, H., Nulsen, P. E. J., & Fabian, A. C. 1984, MNRAS, 208, 261
Thomas, D., Greggio, L., & Bender, R. 1999, MNRAS, 302, 537
Tinsley, B. M., & Larson, R. B. 1979, MNRAS, 186, 503
Tojeiro, R., Heavens, A. F., Jimenez, R., & Panter, B. 2007, MNRAS, 381, 1252
Toomre, A. 1977, in Evolution of Galaxies and Stellar Populations, ed. B. M. Tinsley, R. B. G. Larson, & D. Campbell (New Haven, CT: Yale University Press), 407
Valluri, M. 1993, ApJ, 408, 57
Vazdekis, A., Sánchez-Blázquez, P., Falcón-Barroso, J., et al. 2010, MNRAS, 404, 1639
Verstappen, J., Fritz, J., Baes, M., et al. 2013, A&A, 556, A54
Vollmer, B., Cayatte, V., Balkowski, C., & Duschl, W. J. 2001, ApJ, 561, 708
Vulcani, B., Poggianti, B. M., Fritz, J., et al. 2015, ApJ, 798, 52
Wallerstein, G. 1962, ApJS, 6, 407
Weinberg, M. D. 1985, MNRAS, 213, 451
Weiner, B. J., Papovich, C., Bundy, K., et al. 2007, ApJL, 660, L39
Wilkinson, D. M., Maraston, C., Thomas, D., et al. 2015, MNRAS, 449, 328
Wuyts, S., Förster Schreiber, N. M., Nelson, E. J., et al. 2013, ApJ, 779, 135